Luminosity distance uncertainties from gravitational wave detections of binary neutron stars by third generation observatories

Josiel Mendonça Soares de Souza[*]

Departamento de Física Teórica e Experimental, Universidade Federal do Rio Grande do Norte, Natal-RN 59072-970, Brazil

Riccardo Sturani[†]

Instituto de Física Teórica, UNESP-Universidade Estadual Paulista & ICTP South American Institute for Fundamental Research, São Paulo 01140-070, SP, Brazil

A new generation of terrestrial gravitational wave detectors is currently being planned for the next decade, and it is expected to detect most of the coalescences of compact objects in the Universe with masses up to a thousand times the solar mass. Among the several possible applications of current and future detections, we focus on the impact to the measure of the luminosity distance of the sources, which is an invaluable tool for constraining the cosmic expansion history of the Universe. We study two specific detector topologies, triangular and L-shaped, by investigating how the topology and relative orientation of up to three detectors can minimize the uncertainty measure of the luminosity distance. While the precision of the distance measurement is correlated with several geometric angles determining the source position and orientation, focusing on the bright standard sirens and assuming a redshift to be measured with high accuracy, we obtain analytic and numerical results for its uncertainty, depending on the type and number of detectors composing a network, as well as on the inclination angle of the binary plane with respect to the wave propagation direction. We also analyze the best relative location and orientation of two third generation detectors to minimize the luminosity distance uncertainty, showing that prior knowledge of the inclination angle distribution plays an important role in the precision recovery of luminosity distance and that a suitably arranged network of detectors can drastically reduce the uncertainty measure, approaching the limit imposed by lensing effects intervening between source and detector at a redshift $z \gtrsim 0.7$.

I. INTRODUCTION

While still in its infancy, gravitational wave (GW) astronomy is already providing observational data [1–3] of invaluable importance as well as testing the fundamental nature of gravity [4,5] and cosmology [6–8].

Second generation (2G) detectors LIGO [9] and Virgo [10] collected signals from coalescing binaries at the rate of $O(1)$ event per week during their third observation run, and a similar or large rate is expected for future observations runs that are presently happening or in the near future [11], when the Japanese detector KAGRA will also be part of the observational network [12].

The GW detections from coalescing binaries impacted on several fields in physics, and in this work, we focus on the determination of the *luminosity distance* of their sources, which is a crucial ingredient to reconstruct the cosmic expansion history.

As is well known [13,14], coalescing binaries are *standard sirens*; i.e., their characteristic chirp signal enables an absolute calibration of the gravitational luminosity, leading to an unbiased determination of the luminosity distance, which, together with the redshift, are the two observables necessary to determine the cosmic expansion history of the Universe. However redshift is in general not provided by GW detections, but it can be obtained by the host galaxy identification, which is possible for electromagnetically (EM) *bright* standard sirens. The most likely case, although not exclusive, see, e.g., [15–21], of GW signal accompanied by an EM counterpart is given by binary neutron star systems with a mass ratio close to unity, for which tidal forces are larger [22].[1] In the case the neutron star is tidally disrupted outside the effective innermost stable orbit of the binary, material is ejected from the system and is expected to produce an EM

---

[*]josiel.mendonca.064@ufrn.edu.br
[†]riccardo.sturani@unesp.br

---

[1]Tidal forces in the final stage of the inspiral are inversely proportional to the (square) mass of the object sourcing the tidal field.
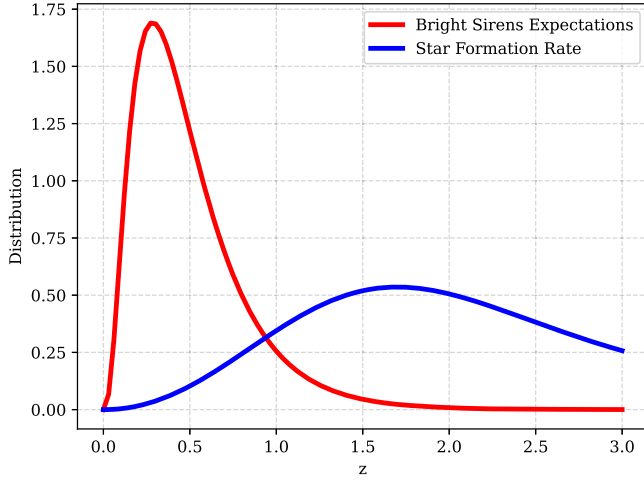
FIG. 1. Expected redshift distribution of bright standard sirens assuming an electromagnetic counterpart is detected by Theseus [37], compared with observed star formation rate [40].

counterpart [21], in particular a short gamma ray burst and a kilonova, besides a lower frequency emission lasting up to years [21,23].

For reference, GW-determined sky localization areas encompassed $\Delta\Omega$ of, say, $\sim$16–few $\times 10^3$ deg^2 in recent detections [1–3]. Up to a distance of 100 Mpc, the number of galaxies N_{100} included in a sky region of area $\Delta\Omega$ is roughly $N_{100} \sim 5 \times \Delta\Omega/(10 \text{ deg}^2)$, assuming the average Milky-Way-like galaxy density to be $\sim$5 $\times 10^{-3}$ Mpc^{-3} [24].

Events collected so far by 2G detectors show an overwhelming majority of binary black holes over binary systems involving at least one neutron star. In only one case, the notable binary neutron star (BNS) system that sourced GW170817 [25], the GW signal was accompanied by EM counterparts, with consequent host galaxy identification and redshift determination. While several methods have been proposed and used to get redshift information

from EM-dark GW detections, using, e.g., statistical identification of host galaxy [26–28], full cross-correlation with galaxy catalogs [8,29,30], statistical redshift distribution of sources [31,32], features in the black hole mass spectrum [33], neutron star tidal effects imprinted in the waveform [34], the golden events having the individually highest constraining power over the cosmic expansion history are EM-bright standard sirens, where host galaxy identification enable a redshift determination with negligible error [35].

For third generation (3G) detectors, most of the BNS coalescences will be visible [36], but the EM counterparts are not expected to be detected beyond a limiting redshift $\bar{z} \simeq 0.7$, with the bulk of the distribution of bright standard sirens expected around $z \sim 0.3$–0.4 [37,38], making most of them invisible to 2G detectors [39]; see Fig. 1.

The 3G detectors are currently under active research and development, and in the present work, we will assume that the Einstein Telescope (ET) will be a triangular interferometer with arms at 60° degrees [41], and the Cosmic Explorer (CE) a single L-shaped interferometer [42] with arms at 90°, with a dimensionless noise characteristic strain $h_c = \sqrt{fS_n}$ displayed in Fig. 2, S_n being the standard single sided noise spectral density, see, e.g., Chap. 7 of [43], while analogue quantities for 2G detectors can be found in [44].

Within this context, we investigate the relative configuration of ET-like and CE-like detectors that maximizes the accuracy on the luminosity distance determination of binary neutron stars, taking into account statistical features of the sources like inclination angle distribution.

The paper is organized as follows. In Sec. II, we lay out the tools employed to quantitatively analyze luminosity distance measures in EM-bright GW detections by the 3G detectors mentioned above, with the results presented in Sec. III. Section IV contains the conclusions that can be drawn from our study.
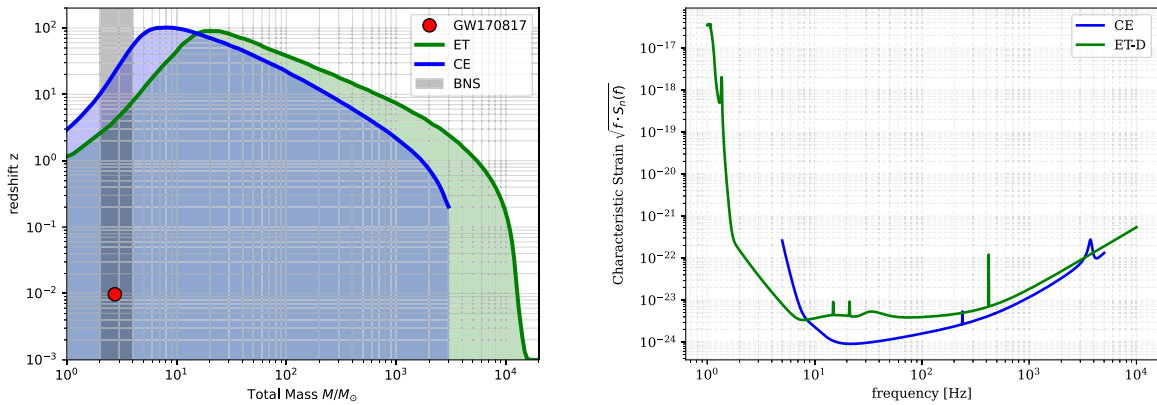
FIG. 2. Left: Luminosity distance reach for equal mass, nonspinning system, assuming fundamental $l = m = 2$ mode only, for optimally oriented binaries, given the spectral noise density S_n [45,46] for CE and [ET-D] from [47] for ET. The mass and luminosity distance of GW170817 are highlighted, as well as the mass region where BNSs are expected. Right: Dimensionless noise characteristic strain h_c, defined in terms of spectral noise $h_c \equiv \sqrt{fS_n}$ for L-shaped CE and triangle-shaped ET.
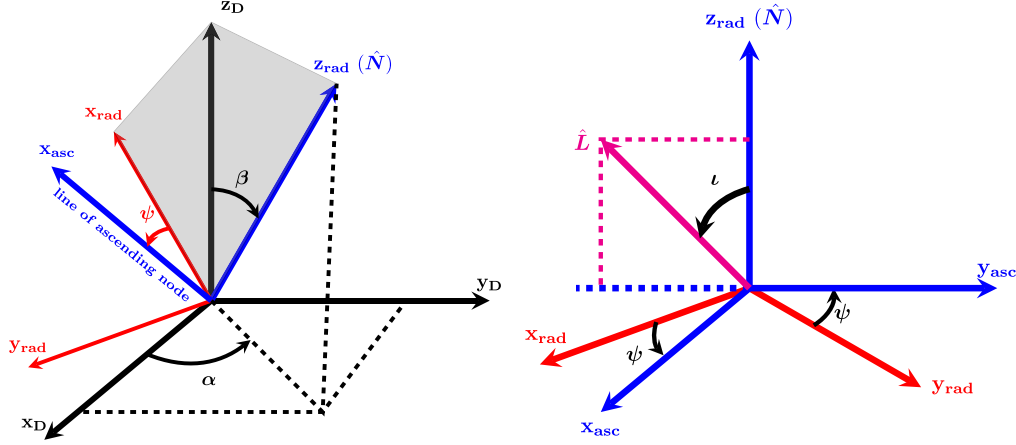
FIG. 3.   Schematic representation of detector geometry and of radiation frame.

II. METHOD

A. Basics

Gravitational radiation in general relativity is endowed with two polarizations, conventionally indicated by h_+ and $h_\times$, which can be suitably decomposed into modes using spin-weighted spherical harmonics $^{-s}Y_{lm}$ of weight $s = -2$, according to

$$h_+ - ih_\times = \frac{GM}{r} \sum_{l \geq 2} \sum_{|m| \leq l} H_{lm}{}^{-2}Y_{lm}(\iota, \phi), \qquad (1)$$

where Newton constant G, total rest mass M of the source, and coordinate distance of the source to the observer r have been factored out. The luminosity distance d_L is related to r and the redshift z via $d_L = (1 + z)r$. Applying Eq. (1) to the case of a binary system, ι denotes the angle between the unit vector perpendicular to the binary plane $\hat{L}$ and the radiation direction parametrized by the unit vector $\hat{N}$; ϕ parametrizes a rotation in the binary plane.

The expansion coefficients H_{lm} are complex functions of the intrinsic parameters and the retarded time $t - r$. Detector d_i output contain GW signals h_{d_i}, which are linear combinations of the GW polarizations weighted by the *pattern functions* $F_{+,\times}$,

$$h_{d_i} = F_+(\alpha_i, \beta_i, \psi_i)h_+ + F_\times(\alpha_i, \beta_i, \psi_i)h_\times, \qquad (2)$$

where α_i, β_i are detector dependent angles determined by the sky position of the source, and the polarization angles ψ_i can be interpreted as the additional angle (beside ι) relating $\hat{L}$ to $\hat{N}$ [48]. Together ψ_i, ι, and ϕ compose the *Euler angles* determining the relative orientation between *source frame* (defined by the orbital plane and its normal $\hat{L}$) and the *radiation frame* whose $\hat{z}_{rad}$ axis is the unit vector $\hat{N}$ and whose $\hat{x}_{rad} - \hat{z}_{rad}$ plane contains the normal to the detector's plane $\hat{z}_i$; see Appendix A for detailed definition and properties of the polarization angle.

The pattern functions $F_{+,\times}$ can be written as

$$F_+(\alpha_i, \beta_i, \psi_i) = \cos(2\psi_i)f_+(\alpha_i, \beta_i) - \sin(2\psi_i)f_\times(\alpha_i, \beta_i),$$
$$F_\times(\alpha_i, \beta_i, \psi_i) = \cos(2\psi_i)f_\times(\alpha_i, \beta_i) + \sin(2\psi_i)f_+(\alpha_i, \beta_i),$$
$$(3)$$

with $f_{+,\times}$ defined as

$$f_+(\alpha_i, \beta_i) \equiv -\sin(\Omega)\frac{1}{2}(1 + \cos^2\beta_i)\sin(2\alpha_i),$$
$$f_\times(\alpha_i, \beta_i) \equiv -\sin(\Omega)\cos\beta_i\cos(2\alpha_i), \qquad (4)$$

where β_i is (the complement of) the source elevation and the azimuth angle α_i is measured with respect to the bisector of the angle formed by the interferometer's arms. The pattern functions (4) can be obtained by projecting the gravitational perturbation tensor onto the interferometer response tensor $\frac{1}{2}(u^iu^j - v^iv^j)$, with $\hat{u}, \hat{v}$ being the unit vector pointing along the detector's arms, and allowing for the possibility of a variable opening angle Ω between them; see Fig. 3.[2]

As per standard treatment, the detectors' output h_{d_i} is processed via *matched filtering* [49], which consists in taking a noise-weighted correlation of the data with a precomputed waveform model, or *template* h_t, according to[3]

$$\langle h_{d_i}, h_{t_i}\rangle(t_i)$$
$$\equiv 2\int_0^\infty \frac{[\tilde{h}_{d_i}(f)\tilde{h}_{t_i}^*(f)e^{-2i\pi f t_i} + \tilde{h}_{d_i}^*(f)\tilde{h}_{t_i}(f)e^{2i\pi f t_i}]}{S_{n_i}(f)}df,$$
$$(5)$$

---

[2]We understand the Ω dependence in the notation of $f_{+,\times}$. For all applications, we will use $\Omega = \pi/2$ for L-shaped (CE-like) interferometers and $\Omega = \pi/3$ for triangle-shaped (ET-like) ones.

[3]We adopt the convention $\tilde{g}(f) = \int g(t)e^{2i\pi f t}dt$.

whose output is the time-dependent correlation between data and the specific template h_{t_i} translated in time by the detector dependent quantity t_i. $S_n(f)$ is the noise spectral density defined in term of detector noise $\tilde{n}(f)$ averaged over many realizations,

$$\langle \tilde{n}(f)\tilde{n}(f')\rangle = \frac{1}{2} S_n(f)\delta(f+f'). \tag{6}$$

The correlation in Eq. (5) can be used to define a scalar product $\langle h_1|h_2\rangle \equiv \langle h_1,h_2\rangle(0)$ and consequently, a norm $\|h\| \equiv \sqrt{\langle h|h\rangle}$.

Searches for maximum matched-filtering output by varying the templates lead to the determination of the best fit waveform and, in a Bayesian inference scheme, to probability distribution functions for all waveform template parameters. Note that the binary constituent masses m_i that can be recovered are the so-called *redshifted*, or *detector* ones, related to intrinsic, or source ones $m_i^{(s)}$ via $m_i = m_i^{(s)}(1+z)$[13]. Optimal matched-filtering leads to the definition of signal-to-noise ratio of signal h (SNR$_h$),

$$\text{SNR}_h^2 \equiv \langle h|h\rangle = 4\int_0^\infty \frac{|\tilde{h}(f)|^2}{S_n(f)}\,df. \tag{7}$$

Focusing on the fundamental mode, i.e., taking the contribution only from $l=2=|m|$ in (1), the signal from the inspiral phase admits a simple analytic description,

$$\tilde{h}_+ = \frac{(1+\cos^2\iota)}{2}h_0(f)e^{i\Phi_{gw}(f)},$$
$$\tilde{h}_\times = i\cos\iota h_0(f)e^{i\Phi_{gw}(f)}, \tag{8}$$

where for $h_0(f)$, the analytic expression is known analytically for the inspiral in the *stationary phase approximation* [50],

$$h_{0\text{insp}}(f) \equiv \left(\frac{5}{24}\right)^{1/2}\pi^{-2/3}\frac{(GM_c)^{5/6}f^{-7/6}}{d_L}, \tag{9}$$

with $M \equiv m_1 + m_2$, $M_c \equiv \nu^{3/5}M$, $\nu \equiv m_1 m_2/M^2$. Similarly, the f-domain phase $\Phi_{gw}(f)$ has a well-known analytic, perturbative representation for the *inspiral* phase of the ith detector,

$$\Phi_{gw_i-\text{insp}}(f) - 2\pi f t_i + \phi_0 + \frac{\pi}{4} \simeq \frac{3}{128\nu v^5}[1+O(v^2)]$$
$$= \frac{3}{128(\pi GM_c f)^{5/3}}[1+O(v^2)], \tag{10}$$

where the quantity $(\Phi_{gw_i-\text{insp}} - 2\pi f t_i)$ is independent of the detector (t_i is the arrival time at the ith detector), the small parameter of expansion in Eq. (10) is $v \equiv (\pi GMf)^{1/3}$, and ϕ_0 a constant phase.

TABLE I. Parameters defining the observation of a binary system observation (whose constituents are treated as a pointlike object) divided between intrinsic ($\vec{S}_{1,2}$ are the binary constituent spin vectors) and extrinsic (t denotes the arrival time), according to the distinction introduced in [51]. In bold are those we searched over via Bayesian inference (d_L, ψ, ι); in gray is the one marginalized over (ϕ).

Intrinsic parameters	Extrinsic parameters
M_c, ν, $\vec{S}_1$, $\vec{S}_2$	**d_L**, **ψ**, **ι**, ϕ, α, β, t

Out of the 15 parameters needed to determine the signal imprinted into a detector by a GW source made of a binary system in circular motion, see Table I, we are interested in the precision of luminosity distance determination of EM bright standard sirens, for which we assume that sky position and consequently, the host galaxy and then the redshift, can be determined with negligible uncertainty.

As explained in the Introduction, we focus our analysis on equal mass binary neutron stars, which are obvious candidates (even if not exclusive) to produce GW signals with an EM counterpart. We will make the additional simplifying assumptions that binary constituent spins can be neglected, as neutron stars in binaries are observed to have in general negligible spins, with values $\lesssim 0.05 m_i^2$ [52]. The remaining intrinsic parameters, the individual masses, are expected to be measured with subpercent accuracy, as happened for GW170817 [25],[4] and as confirmed in general by Fisher matrix analysis for 3G detectors [53].[5]

Matched-filtering technique can provide a very accurate determination in general of the intrinsic parameters, in particular the chirp mass M_c can be determined with the accuracy [54],

$$\frac{\delta M_c}{M_c} \sim \frac{1}{N_{\text{cyc}}} \times \frac{10}{\text{SNR}}, \tag{11}$$

where besides the factor SNR^{-1} usually obtained in a Fisher matrix approximation, one has a N_{cyc}^{-1} uncertainty decrease with an increasing number of observed cycles N_{cyc} from the phase Φ_{gw} dependence on M_c, and the numerical factor ~ 10 is due to correlation with the other mass parameter ν, which enters Eq. (10) beyond leading order.

We further neglect in our Bayesian inference search the arrival time t_i, which is usually obtained with $\sim msec$ accuracy [2] and concentrate on the parameters that have a

---

[4]For reference, the luminosity distance of GW170817 has been measured with $\sim 20\%$ accuracy, and it had a network SNR$_{net}$, i.e., the SNR summed over three detectors of SNR$_{net} = (\sum_{i=1}^3 \text{SNR}_{d_i}^2)^{1/2} \sim 32$.

[5]In particular, in Fig. 13 of [53], it is shown that about 99% of binary neutron star detections by both 2G and 3G detectors will have individual masses accuracy below 0.1%.

larger correlation with the luminosity distance, hence have stronger impact on its recovery value precision.

Note that also calibration errors can affect the measure of luminosity distance, and a proxy for the threshold at which relative calibration error Δ_c become comparable with statistical ones is $\Delta_c \sim 1/\mathrm{SNR}$ [55]. While GW signals from binary neutron stars can reach SNR of 10^3 in 3G detectors [56], the bulk of their distribution will lie at a SNR $\lesssim$ few $\times$ 10 [53]. For this reason, projecting to 3G detectors the Advanced LIGO systematic calibration error in the first half of the third observation run, estimated $< 2\%$ [57], one can assume that calibration uncertainty should not affect the overwhelming majority of signals we are discussing.

According to Eq. (2), detectors with different orientations measure different combinations of h_+ and $h_\times$; hence, in principle, with two or more detectors, it is possible to disentangle the $\iota - d_L$ degeneracy. However, the two LIGOs are oriented to have very similar pattern functions (apart from a sign), [58] and in the GW170817 case, very little SNR was present in the remaining detector of the network, Virgo [25].

Another element that can break the degeneracy is the presence in the signal of a significant contribution from subdominant modes with $l > 2$, which are weighted by a different function of ι than the $l = 2$, $|m| = 2$ mode determined by Eq. (8). However subdominant modes are not expected to be seen in GWs emitted by binary neutron stars, whose part of the signal visible in the detectors is in the inspiral phase[6] for which subdominant modes are suppressed by powers of the relative binary constituent velocity as v^{l-2}. Moreover, odd higher modes vanish in the limit $m_1 = m_2$; hence, they are suppressed for comparable masses, and in general, subdominant modes are more important for edge-on viewing angles, i.e., $\iota \sim \pi/2$ [59]. We will come back on source ι distribution in Sec. III B.

B. Cutler-Flanagan parametrization

Crucial roles to estimate the luminosity distance measurement uncertainty are played by detector topology, location, and orientation, and we find it convenient to investigate this issue using the parametrization of the signal introduced in [60]. For a single detector d_i, denoting $v \equiv \cos\iota$, $\chi_+ \equiv (1 + v^2)/2$ (and $\chi_\times \equiv -iv$ for future reference), one can write the SNR as

$$\mathrm{SNR}_i^2 = 2(f_{+i}^2 + f_{\times i}^2)\{(\chi_+^2 + v^2) + (\chi_+^2 - v^2)\cos[4(\psi_i + \bar{\psi}_i)]\}\int_0^\infty \frac{|h_0(f)|^2}{S_{n_i}(f)}df$$

$$= 2(f_{+i}^2 + f_{\times i}^2)(\chi_+^2 + v^2)[1 + f(v)\cos(4(\psi_0 + \delta\psi_i + \bar{\psi}_i))]\int_0^\infty \frac{|h_0(f)|^2}{S_{n_i}(f)}df, \qquad (12)$$

where we have used the detector's output Eq. (2) in the SNR expression (7). The newly introduced quantity $\bar{\psi}_i$ is defined via

$$\cos(4\bar{\psi}_i) \equiv \frac{f_{+i}^2 - f_{\times i}^2}{f_{+i}^2 + f_{\times i}^2}, \qquad \sin(4\bar{\psi}_i) \equiv \frac{2f_{+i}f_{\times i}}{f_{+i}^2 + f_{\times i}^2}, \quad (13)$$

and in the second line of Eq. (12), we have written $\psi_i = \psi_0 + \delta\psi_i$, where ψ_0 is the polarization angle relative to the Earth north pole unit vector $\hat{z}_0$ [i.e., using $\hat{z}_0$ for $\hat{z}_i$ in Eq. (A3), $\delta\psi_i$ being defined as a consequence]. Finally, we adopted the notation,

$$f(v) \equiv \frac{\chi_+^2 - v^2}{\chi_+^2 + v^2} = \frac{(1 - v^2)^2}{1 + 6v^2 + v^4}. \qquad (14)$$

The pattern functions $f_{+i,\times i}$ depend on a detector location via their arguments (α_i, β_i) as per Eq. (4); $\delta\psi_i$ depends on the source location with respect to the detector, but it has

the nontrivial property of not depending on the polarization angle, see Appendix A.

The main advantage of the SNR formulation in Eq. (12) is that it separates the contribution to the SNR into a part that depends on the polarization angle ψ and a part that is ψ independent. In general, it is difficult to recover ψ, and its uncertainty affects the measure of the SNR, see Eq. (21), hence, jeopardizing the precision of d_L.

Given that the polarization angle parametrizes rotations in the $+, \times$ space, the signal in each detector can be elegantly written in terms of quadratic forms via

$$\tilde{h}_{d_i} = h_0(f)e^{i\Phi_{gw_i}}V_A(v)R_{AB}(2\psi_0)R_{BC}(2\delta\psi_i)f_{Ci}$$
$$= h_0(f)\mathcal{A}_A R_{AB}(2\delta\psi_i)f_{Bi}e^{2\pi i f t_i}, \qquad (15)$$

where capital Latin indices A, B, C run over $\{+, \times\}$, R_{AB} is the standard 2×2 rotation matrix,

$$R_{AB}(\alpha) \equiv \begin{pmatrix} \cos\alpha & -\sin\alpha \\ \sin\alpha & \cos\alpha \end{pmatrix}. \qquad (16)$$

We have collected in a two-vector, the dependence of the GW polarizations on ι, i.e., $V_A(v) \equiv (\chi_+, \chi_\times)$, and in the

---

[6]For reference, the inner most stable circular orbit for a spinless, equal mass binary system, corresponds to a GW frequency $f_{\mathrm{GW}} \simeq 730$ Hz$[M/(3M_\odot)]^{-1}$.

second line of Eq. (15), we have defined the detector independent quantity $\mathcal{A}_A(v, \psi_0) \equiv V_B(v) R_{BA}(2\psi_0) e^{i\Phi_{gw}}$. The rationale of this parametrization is to separate parameters which for a given signal are common to all detectors $[h_0(f)\mathcal{A}_A]$, from those depending on the detector $R_{AB}(2\delta\psi_i) f_{Bi} e^{2\pi i f t_i}$.

Following [54], it is possible to generalize the SNR parametrization of Eq. (12) to the case of a network made of n_{det} detectors,

$$\text{SNR}^2_{\text{net}} \equiv \sum_{i=1}^{n_{\text{det}}} \text{SNR}^2_i$$
$$= \text{SNR}^2_0 \mathcal{R}eal[\mathcal{A}^*_A(v, \psi_0) \mathcal{A}_B(v, \psi_0)] \sum_{i=1}^{n_{\text{det}}} \Xi_{ABi},$$

(17)

with

$$\Xi_{ABi} \equiv R_{AC}(2\delta\psi_i) R_{BD}(2\delta\psi_i) f_{Ci} f_{Di} \omega_i,$$
$$\omega_i \equiv \frac{\int_0^\infty |h_0(f)|^2 S_{n_i}^{-1}(f) df}{\int_0^\infty |h_0(f)|^2 S_{n_{\text{avg}}}^{-1}(f) df},$$
$$\text{SNR}^2_0 \equiv 4 \int_0^\infty df \frac{|h_0(f)|^2}{S_{n_{\text{avg}}}(f)},$$
$$S_{n_{\text{avg}}}^{-1}(f) \equiv \frac{1}{n_{\text{det}}} \sum_i S_{ni}^{-1}(f).$$

(18)

One can then define a symmetric 2×2 matrix Ξ_{AB}, which can be diagonalized by a suitable rotation matrix of the type (16) with an angle $\bar{\psi}$, as

$$\Xi_{AB} \equiv \sum_i \Xi_{ABi} = \sum_i R_{AC}(2\bar{\psi}) \bar{\Xi}_{CD} R_{DB}(2\bar{\psi}), \quad (19)$$

whose explicit expression is reported in Appendix A. It is convenient to parametrize the 2 degrees of freedom of diagonal matrix $\bar{\Xi}_{AB}$ as

$$\bar{\Xi}_{AB} = \sigma \begin{pmatrix} 1 + \epsilon & 0 \\ 0 & 1 - \epsilon \end{pmatrix}, \quad (20)$$

with $\sigma = \frac{1}{2}(\Xi_{++} + \Xi_{\times\times})$ and $\epsilon = \sqrt{(\Xi_{++} - \Xi_{\times\times})^2 + 4\Xi_{+\times}^2}/(\Xi_{++} + \Xi_{\times\times})$, which is bounded by $0 \le \epsilon \le 1$. In the particular case of a single detector, one has that $\epsilon = 1$ (and $\omega_1 = 1$), as each Ξ_{ABi} has vanishing determinant, being the outer product of two copies of the same vector.

For a generic detector network, the combined $\text{SNR}^2_{\text{net}}$ of Eq. (17) can then be written as

$$\text{SNR}^2_{\text{net}} = \text{SNR}^2_0 \mathcal{R}eal[\mathcal{A}^*_C R_{CA}(2\bar{\psi}) \bar{\Xi}_{AB} R_{BD}(2\bar{\psi}) \mathcal{A}_D]$$
$$= \text{SNR}^2_0 \sigma[(\chi_+^2 + v^2) + \epsilon(\chi_+^2 - v^2) \cos(4(\psi_0 + \bar{\psi}))].$$

(21)

The quantities σ, ϵ depends on the detector network and on the direction of propagation $\hat{N}$, but they are independent of other angles parametrizing the binary plane orientation (ι, ψ, ϕ). For a fixed detector configuration, ϵ, σ parametrize in a simple way the SNR dependence, which respectively depends and does not depend on the polarization angle ψ. Note that an analogue but not equivalent parametrization has been introduced in [61], whose parametrization allows us to pinpoint the *dominant polarization* mode, i.e., the combination of polarizations that contributes the most to the SNR; see Appendix C.

C. Expected rates

For cosmological applications, it is crucial to have an accurate measure of the luminosity distance, which one can expect to be obtained by using multiple observatories sensitive to different polarization combinations. The rate of an EM bright standard siren is not supposed to exceed $O(1)$ per year with current generation detectors [11]; an estimate for 3G detectors can lead to $O(100)$ per year [37]. As for the expected redshift distribution, an example for EM-bright standard sirens is reported in Fig. 1, where as a reference, is also reported the star formation rate,

$$R_{sfr} = \frac{1}{1 + z} \frac{dV_c}{dz} \psi_{\text{DM}}(z), \quad (22)$$

where ψ_{DM} is the star formation rate taken from [40] and V_c is the comoving volume.[7]

In Fig. 2, we report the luminosity distance reach of BNS for optimally oriented, equal mass, spinless systems (i.e., the distance at which $\text{SNR}_i = 8$) and the design noise curves of CE [42] and ET [62].

In the following section, we show nontrivial consequences that can be deduced from the parametrization in Eq. (21), supporting them with numerical results obtained with Bayesian inference methods.

III. RESULTS

A. The Bayesian setup

In a standard Bayesian inference framework, one has to consider the likelihood

$$\mathcal{L} = e^{-\frac{1}{2}\sum_i \|h_{d_i} - h_{t_i}\|^2}, \quad (23)$$

---

[7]Given the moderate range of expected bright standard sirens, our d_L recovery prior is uniform in comoving volume.

where the norm has been inherited by the scalar product defined implicitly in Eq. (5). We will consider the above likelihood for fixed values of the masses (setting the spins to zero), sky-position angles, and time of the event. This is a reasonable simplification of the problem, assuming that the EM counterpart allowed a precise sky localization and

that the correlation of the detected signal with long templates allowed a precise determination of the arrival time and the masses, which determine the chirping phase of the signal.

By using only the dominant modes $l = |m| = 2$, one can cast the likelihood $\mathcal{L}$ for data d_i into the form,

$$\log \mathcal{L} = -\sum_{i=1}^{n_{\text{det}}} \int_{-\infty}^{\infty} df \frac{|\tilde{h}_{d_i}(f) - \tilde{h}_t(f)|^2}{S_{n_i}(f)}$$

$$= -\sum_{i=1}^{n_{\text{det}}} \int_{-\infty}^{\infty} \frac{df}{S_{n_i}(f)} [|\tilde{h}_{d_i}(f)|^2 + |\tilde{h}_{t_i}(f)|^2 - 2\tilde{R}(f)\cos(2\phi) - 2\tilde{I}(f)\sin(2\phi)], \quad (24)$$

where we have defined $\tilde{R}(f), \tilde{I}(f)$ as, respectively, the real and imaginary part of $\tilde{h}_{d_i}(f)\tilde{h}_{t_i}^*(f)$.

Assuming a flat prior, marginalization over ϕ can be performed analytically using [63,64]

$$\frac{1}{2\pi} \int_0^{2\pi} dx e^{a\cos(x) + b\sin(x)} = I_0\left(\sqrt{a^2 + b^2}\right), \quad (25)$$

where $I_\nu(x)$ is the Bessel function of the first kind of order ν, and the marginalized likelihood $\mathcal{L}_\phi$ will depend only on the extrinsic parameters d_L, ι, and ψ,

$$\mathcal{L}_\phi = \frac{1}{2\pi} \int_0^{2\pi} \mathcal{L} d\phi = \exp\left[-\frac{1}{2} \sum_i^{n_{\text{det}}} (\|h_{d_i}\|^2 + \|h_{t_i}\|^2)\right] I_0\left(2\left|\sum_i^{n_{\text{det}}} \int_{-\infty}^{\infty} df \frac{h_{d_i} h_{t_i \phi=0}^*}{S_{n_i}(f)}\right|\right). \quad (26)$$

When considering the injection data to correlate with templates, we will work in the zero noise approximation [65], as is usually done in the literature to estimate average uncertainties in Gaussian noise.

We run Bilby [66] with the Nestle sampler [67], which implements the nested sampling algorithm [68], with 300 live points, searching over three parameters d_L, ψ, ι. Results for every d_L injection are averaged over the 300 injections simulating random values of α, β, ι, ψ, which survives the SNR cutoff of 8 in each detector.

For the simulation efficiency reason, we used *TaylorF2* waveform model [69] with a fixed total mass $M = 3M_\odot$, equal binary component masses, and no spins. We have also verified in a few cases that no significant deviations occur in the result when replaced with a waveform complete with a merger-ringdown model, like *IMRPhenomD* [70,71]; see the right plot in Fig. 17 for qualitative reference, and we neglected tidal effects.

B. Impact of ι and source location on d_L uncertainty

Expressions (20), (21) permit to highlight the following fundamental features:

(1) For a single detector, $\epsilon = 1$, $\sigma = \frac{1}{2}(f_+^2 + f_\times^2)$, and we recover Eq. (12) [and also Eq. (A8) reduces to Eq. (13)].

(2) For colocated detectors and a source on the top of them, one has $f_+ = f_\times = \sin\Omega$, implying $\sigma = n_{\text{det}}/2 \times \sin^2\Omega$, which is its maximum value.

(3) In the case of a single L-shaped detector ($\epsilon = 1$), the detected signal is a single combination of the two polarizations, and one has no information on the polarization angle. Considering that for a large argument, the Bessel function has $I_0(x) \sim e^x/\sqrt{2\pi x}$; the marginalized likelihood can then be written as

$$-2\log \mathcal{L}_\phi = \sum_{i=1}^{n_{\text{det}}} (\|h_{d_i}\|^2 + \|h_{t_i}\|^2)$$

$$- 2\left[x - \frac{1}{2}\log(2\pi x)\right],$$

$$x \equiv \left|\sum_{i=1}^{n_{\text{det}}} \int_{-\infty}^{\infty} \frac{h_{d_i} h_{t_i \phi=0}^*}{S_{n_i}} df\right|, \quad (27)$$

and the scalar product between the data and template can be decomposed analogously to what was done in Eq. (17) for the SNR,

$$\langle h_{d_i}|h_{t_i}\rangle = \text{SNR}_0^2 \mathcal{R}eal[\mathcal{A}_{d_i A}^* \mathcal{A}_{tB}\Xi_{dt_i AB}], \quad (28)$$
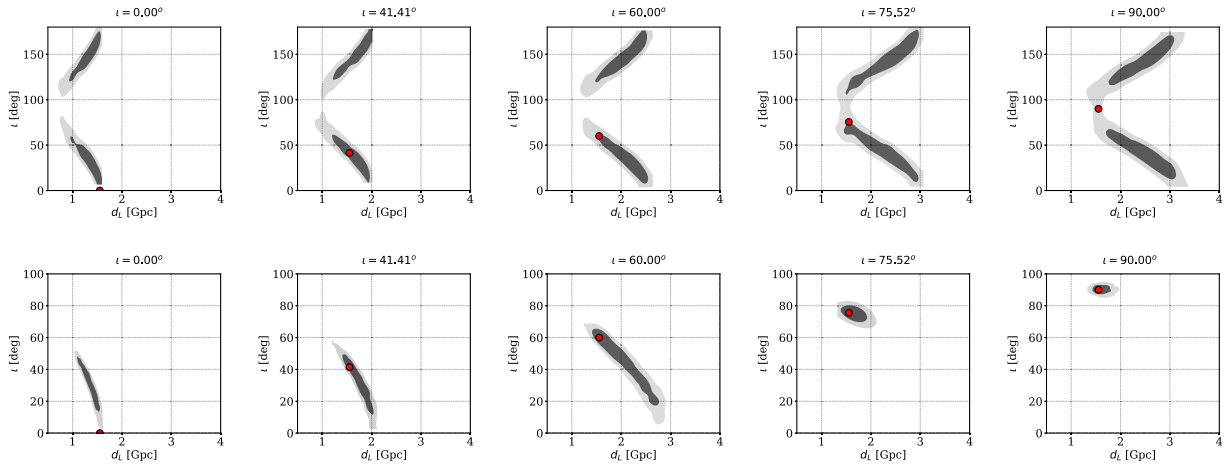
FIG. 4. Examples of two-dimensional PDF for ι vs d_L for a single CE-like, L-shaped interferometer (top) and a triangle-shaped one (bottom) for source parameters giving $\epsilon = 0.0089$ [75]. Note that the volumetric prior at recovery tends to disfavor $\iota \to \pi/2$ for L-shaped detectors.
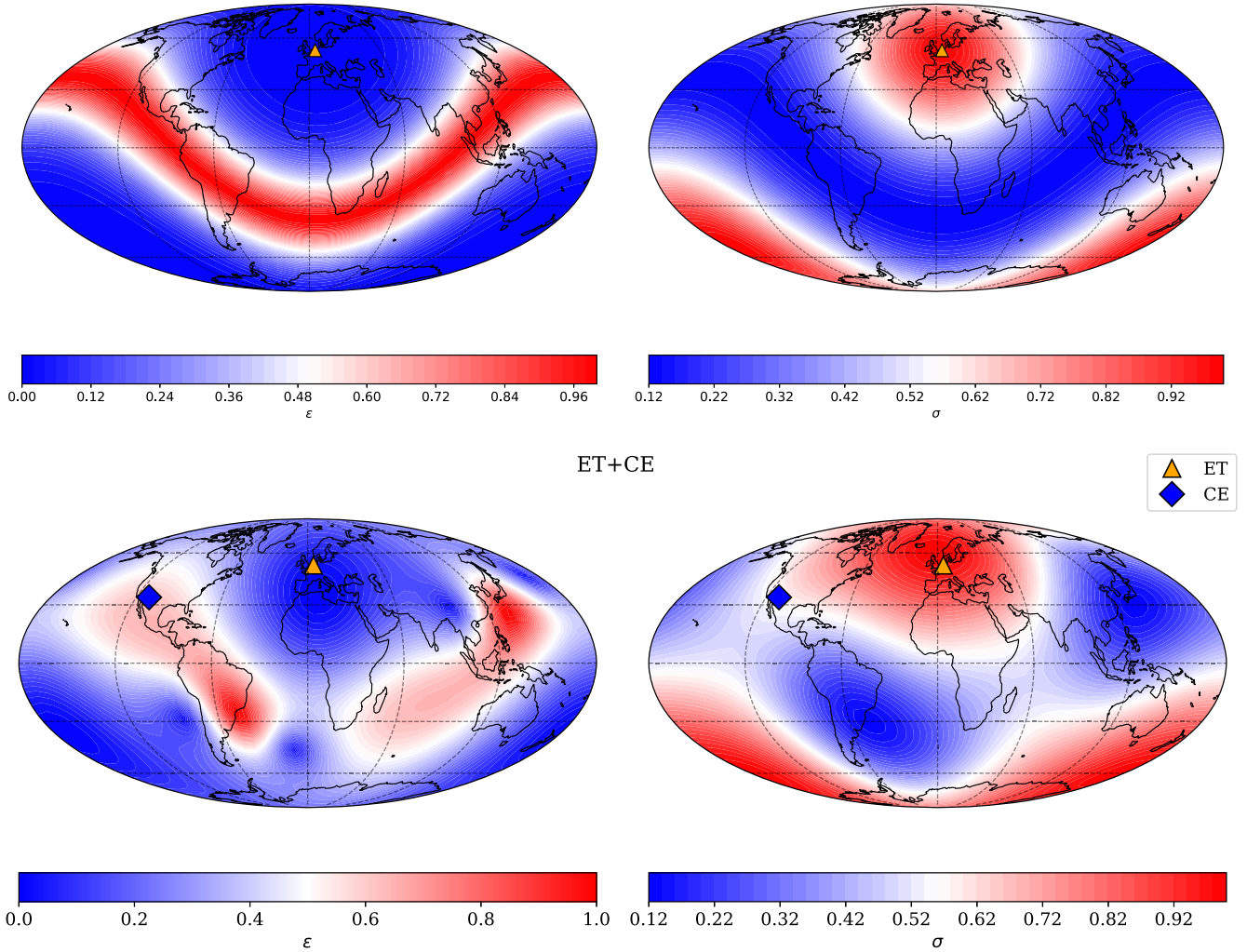
FIG. 5. Values of ϵ (left) and σ (right) for a single ET detector (top, ET location marked with a triangle) and for an ET-CE network (bottom, CE location marked with a diamond).
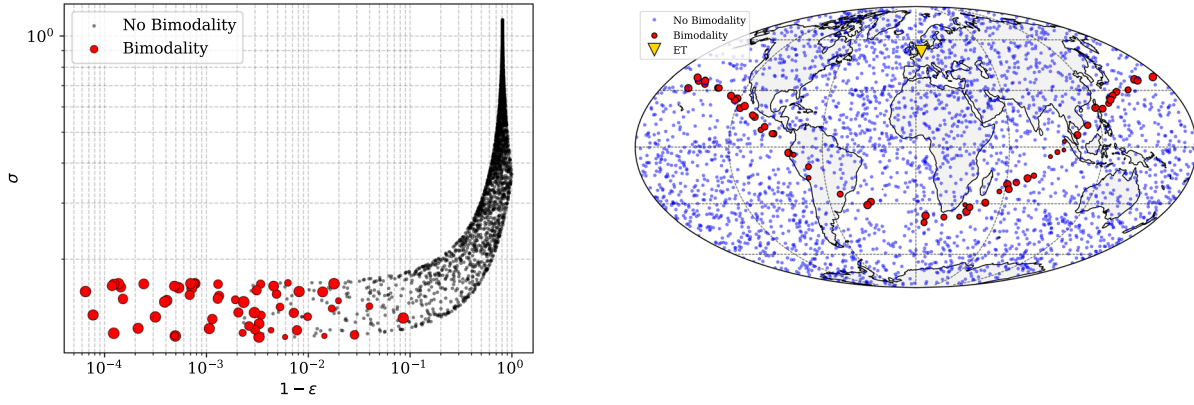
FIG. 6.   Left: Distribution of σ and ϵ values, defined in Eq. (20), for a triangle-shaped interferometer. Right: Points in the sky presenting bimodality are confined to the plane of the detector, where blind directions to individual interferometer appear. Operationally, we defined bimodality to be present when the ratio (smaller or equal to 1) of the height of the peaks of the ι PDF is larger than the PDF value at $\iota = \pi/2$.
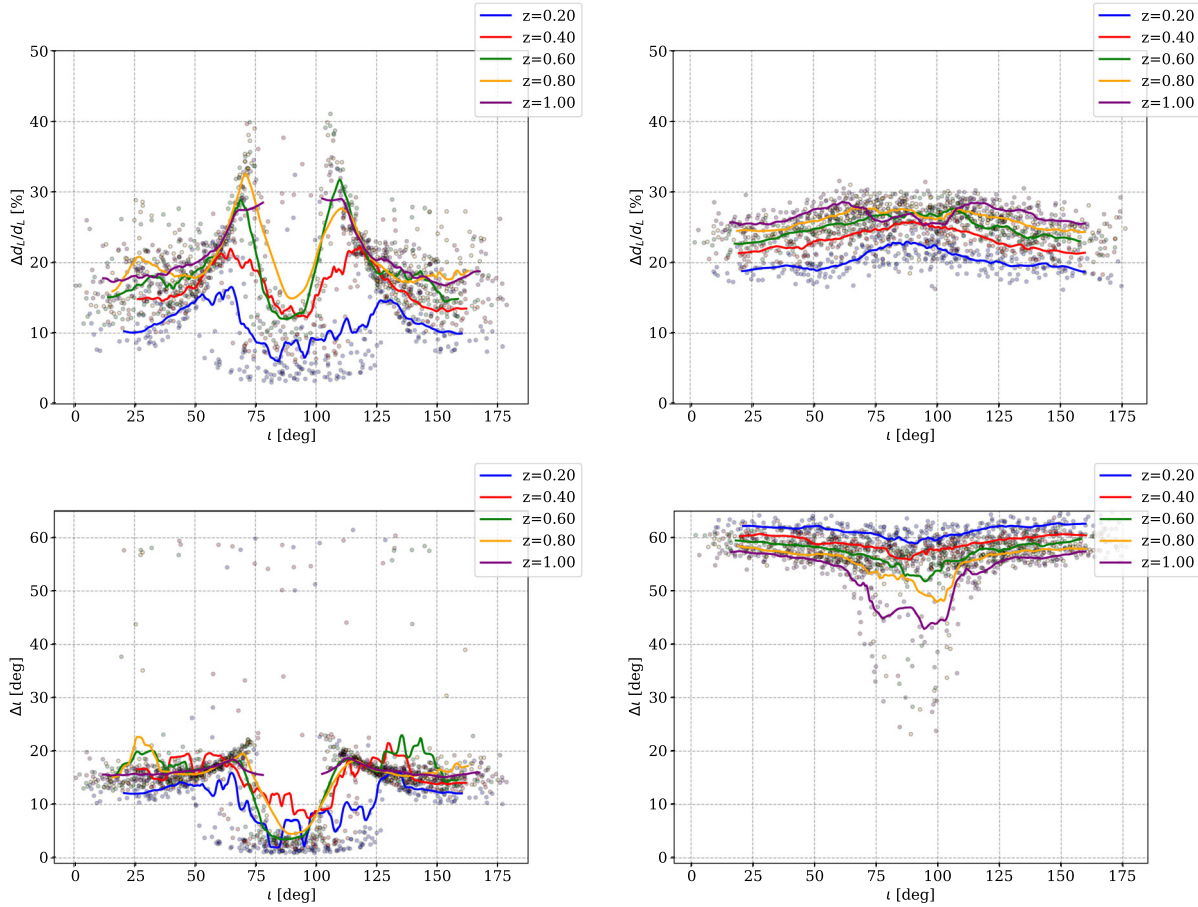
FIG. 7.   Scatter values and averages for relative uncertainty of d_L (top) and absolute one of ι (bottom) as a function of ι for various distances for an ET-like detector (left) and for a single CE one (right), for 300 simulations at each distance. Continuous lines are averages over intervals of 0.1 radians in ι. Note the dip in d_L uncertainty for $\iota \to \pi/2$ in the ET case. The points where CE outperforms ET in Δd_L are due to the better spectral noise sensitivity of the detector, see Fig. 2, hence higher SNR, see Fig. 8. Most of the recovered ι for CE present bimodality ($\Delta\iota \sim 60°$), bimodality that happens far more rarely for ET, as shown by the red dots in the left plot of Fig. 6 compared to the majority of gray points in the bottom right plot here clustering around $\Delta\iota \sim 60°$. For an ET-like detector, there is no dip in d_L uncertainty for $z \sim 1$ as the SNR decrease for $\iota \to \pi/2$ moves the signal below the SNR $= 8$ threshold, whereas for CE injections at $z = 1$ are just above threshold.
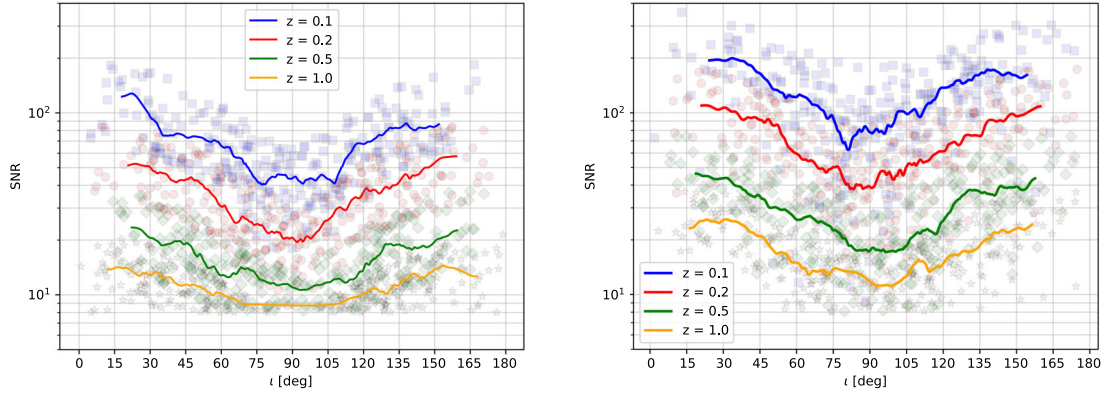
FIG. 8. SNR as a function of ι for various distances for a triangle interferometer (left) and for a single L-shaped detector (right).

where $\Xi_{dt_{i AB}} = R_{AC}(2\delta\psi_{d_i})R_{BD}(2\delta\psi_{t_i})f_C f_D \omega_i$ is the matched-filter analogue of the SNR-related quantity Ξ defined in (17), to which it reduces when the template equals the data. For a single detector $[\omega_i = 1 = \epsilon$, see Eqs. (18) and (19)], the matrix Ξ_{dt_i} is not symmetric but can still be diagonalized into the form,

$$\bar{\Xi}_{dt_{i AB}} = (F_+^2 + F_\times^2)\cos(2(\psi_{d_i} - \psi_{t_i}))\begin{pmatrix} 1 & 0 \\ 0 & 0 \end{pmatrix}, \tag{29}$$

each detector giving a contribution to the log-likelihood,

$$\log\mathcal{L}_{i\phi} \propto 2\sigma\cos(2(\psi_{d_i} - \psi_{t_i})) \\ \times (|\mathcal{A}_{d_i+}|^2 + |\mathcal{A}_{t_i+}|^2 - 2|\mathcal{A}_{d_i+}\mathcal{A}_{t_i+}|), \tag{30}$$

where here with $+, \times$, we denoted the "principal" polarizations diagonalizing $\Xi_{dt_{i AB}}$ [see Appendix A for the matrix diagonalizing $\Xi_{dt_{i AB}}$, and [72] for the version of Eq. (30) not marginalized over ϕ]. Equation (30) indicates that for $\epsilon \sim 1$, the likelihood can constrain only one polarization, leading to the well-known bimodal degeneracy between υ and d_L, as shown in top plots of Fig. 4 for any value of the inclination angle sufficiently away from the $\pi/2$ value.

For a network of interferometers, things are qualitatively different as they are in general sensitive to more than one combination of the two GW-polarizations, and ϵ in Eq. (20) can assume values between 0 and 1, depending on the source location; see Fig. 5. For instance, for a triangle-shaped detector, the condition $\epsilon \sim 1$ is realized only by sources located in a small region of the sky corresponding to the blind (or almost blind) regions of the individual interferometer composing the triangle. They correspond to directions in the plane of the interferometers bisecting their arms, i.e., $\alpha = \Omega/2, \beta = \pi/2$ in Eq. (4). See also Fig. 6 and the additional material in Appendix B, showing that for a value of $\epsilon \sim 1$ and a value of ι sufficiently distant from the symmetric point $\iota = \pi/2$, bimodality appears in the $d_L - \iota$ two-dimensional probability distribution function (PDF). As expected, adding detectors into the network reduces the sizes of $\epsilon \sim 1$ regions; see the bottom of Fig. 5.

(4) It has been empirically noted, e.g., in [72,73], where the sky position is fixed, and [74], where sky localization angles are among the parameters searched for in the Bayesian inference, that for $\iota \sim \pi/2$, the uncertainty in d_L usually drops for triangle-shaped detector; see Fig. 7. Note that the drop in uncertainty while varying ι at a fixed redshift for the triangle-shaped detector is not due to an increase in SNR, which rather *decreases* as $\iota \to \pi/2$,
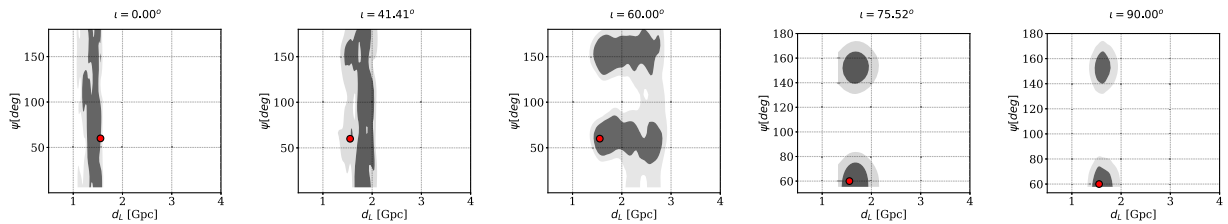
FIG. 9. Examples of two-dimensional PDF for ψ vs d_L for a single triangle-shaped interferometer showing that ψ determination accuracy improves as $\iota \to \pi/2$, as expected from Eq. (21), whose ψ-dependent term is maximum for $\upsilon = 1$, which is $\iota = \pi/2$. The value for ϵ is the same as in Fig. 4.
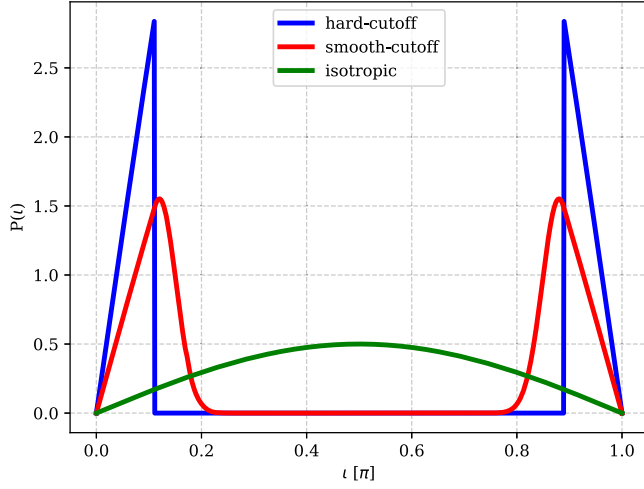
FIG. 10. The three inclination angle distributions for ι used in injections, dubbed "isotropic", "smooth cutoff", "hard cutoff".

as shown in Fig. 8. Actually, it is due to $v \to 0$, leading to the polarization dependent term to become equally important as the non-ψ dependent term in (21). In turn, this leads to a better individuation of the polarizations, as exemplified by Fig. 9. For $z \sim 1$, detections disappear for the triangle-detector as they go below the SNR threshold, while this happens for the L detector at larger distances because of its better sensitivity; see Fig. 2.

For "tropical" inclination angles ($\iota \sim \pi/2$), the ψ-dependent term is as important as the ψ-independent one, with the consequences that while for a L-shaped detector, ψ cannot be constrained, for a triangle-shaped one, a bimodality $d_L - \psi$ appears; see Fig. 9.

Note that while it is more difficult for a CE-like detector to determine ι than for a triangle one, Fig. 7 shows that for specific cases, CE can achieve a better precision due its better sensitivity; see Fig. 2 and top
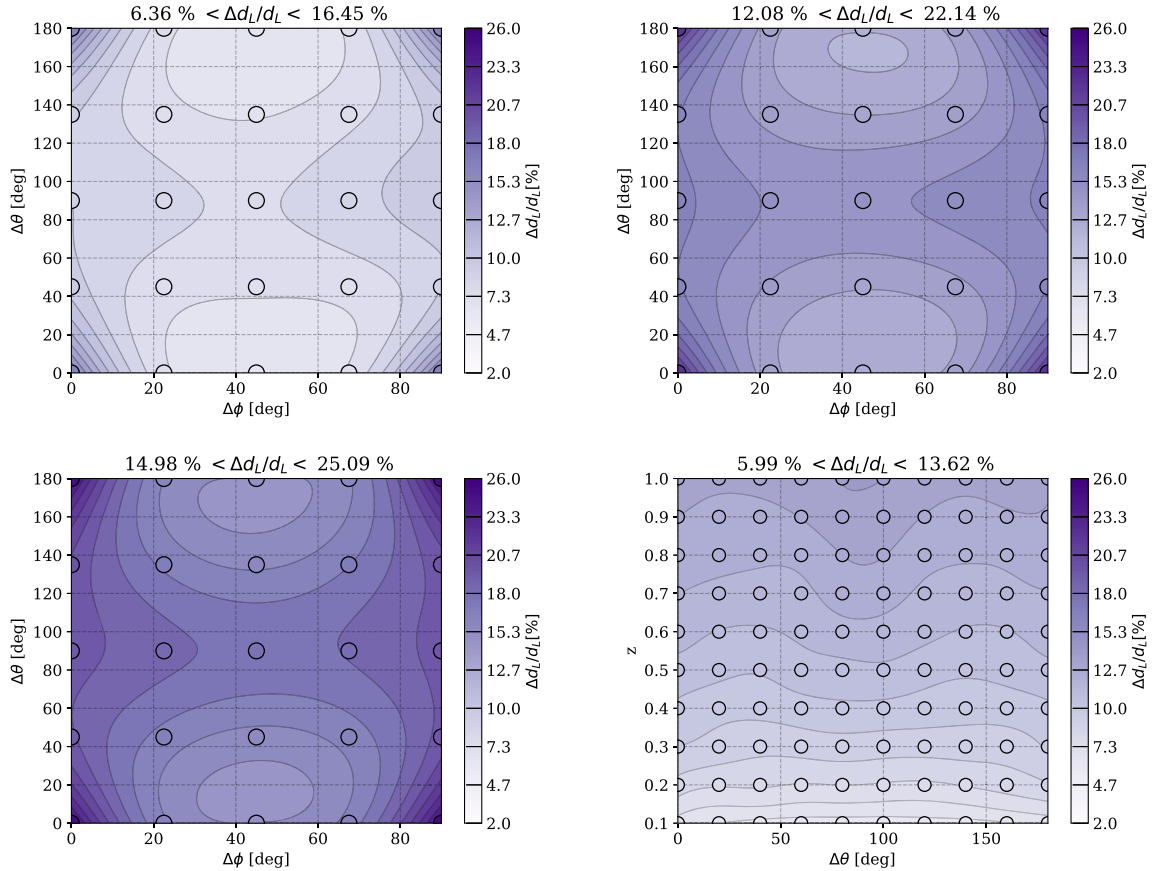
FIG. 11. Error in distance determination averaged over source location, as a function of the angular distance between two 3G detectors. Sources are distributed isotropically in the sky before the SNR$_i > 8$ cut in each detector. Source inclinations are distributed according to *smooth-cutoff* function, see Fig. 10, Bayesian prior for ι at recovery is isotropic. The bottom right plot refers to two ETs, the others to two CEs with sources respectively at $z = 0.1, 0.55, 1$.
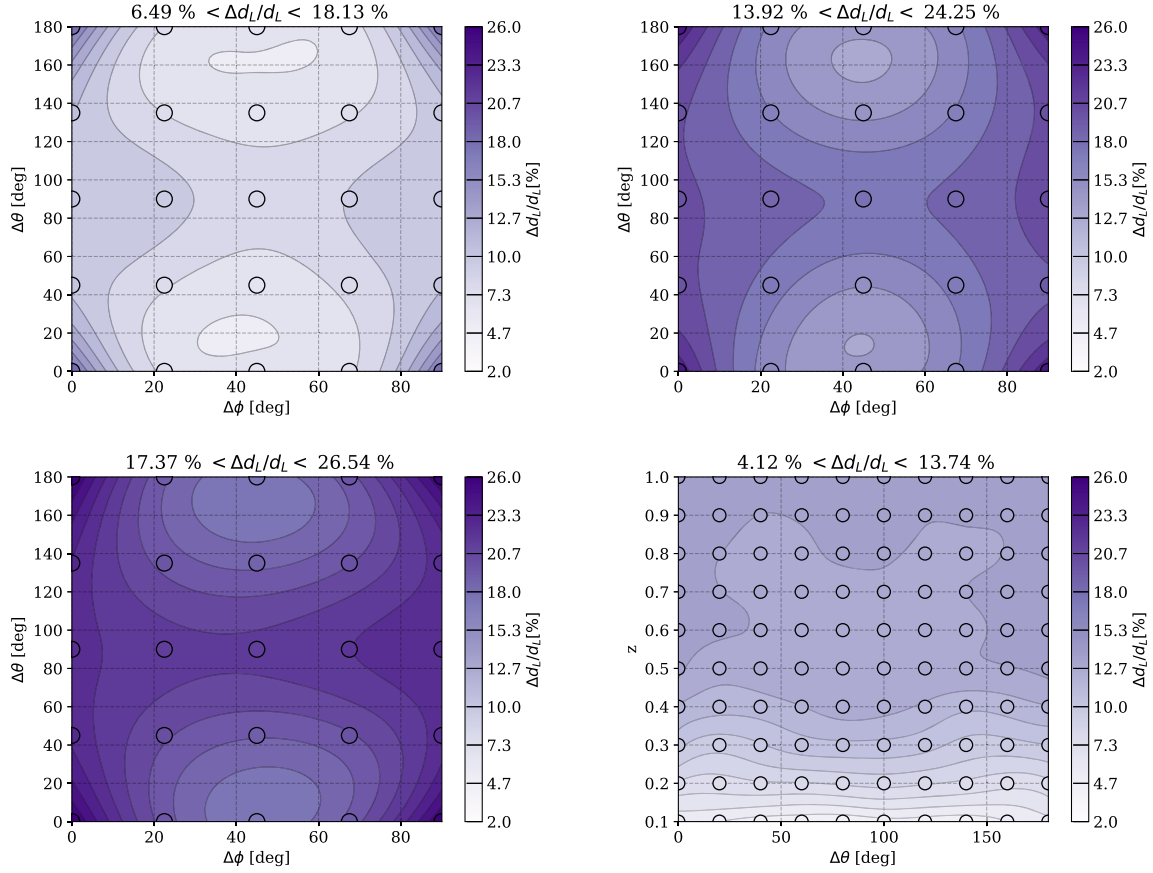
FIG. 12. Same as in Fig. 11 with source inclinations distributed isotropically on the two-sphere.

line in Fig. 8. Note that we used a volumetric prior on d_L, which tends to perform better for $\iota \sim 0$ but which can introduce bias for a L-shaped detector for a "tropical" ι (i.e., $\iota \sim \pi$), as shown by the last top graph in Fig. 4.

C. Impact of detector relative orientation and localization on d_L uncertainty

1. Two detectors

To investigate the best relative location and orientation of two detectors, we place two CE-like detectors on the Earth's surface at an angular distance $\Delta\theta$ one from the other and relative axis orientation $\Delta\phi$, with the result shown in the first three plots of Fig. 11. The signals are simulated with three different distributions of inclination angles, all symmetric for $\iota \to \pi - \iota$, as reported in Fig. 10 (dubbed *isotropic*, *smooth cutoff* and *hard cutoff*) corresponding to the $\hat{L}$ direction being isotropic in the two-sphere, or to ι values concentrated around 0 and π. Signals are produced for sources at three sample values of redshift: $z = 0.1, 0.55, 1$.

The lowest uncertainty is given by detectors either colocated or at antipodal sites, i.e., located on parallel planes, and at a $\Delta\phi = 45°$ degree, so that such a network

will have no blind spots, see Figs. 11,12, which refers respectively to ι of source distributed according to "smooth cutoff" or "isotropic" (there is no difference in the results between "smooth" and "hard cutoff"), and recovered in both cases with an isotropic prior in ι.

In the same Figs. 11 and 12, we also report the result of an analogue exercise with two ET-like detectors, suppressing the coordinate $\Delta\phi$ that does not affect the result. In this case, we find a moderate gain (a few percent) for angular separation $\Delta\theta \simeq 40°$ (or $\Delta\theta \simeq 140°$), which becomes more pronounced at larger redshift, where SNRs are smaller and uncertainties larger.

The differences between Figs. 11 and 12 are minimal, showing that when the prior at recovery is isotropic in the inclination angle ι, the injection distribution in ι has little impact on d_L recovery precision.

2. Three detectors

Finally, we fix the location of an ET-detector and a CE-one, corresponding to an angular distance of 77°. In this case, we verified how the relative luminosity distance uncertainty averaged over source sky location varies with the position of a third ET-like detector, with the results displayed in Fig. 13 for a redshift $z = 0.1, 0.5, 1$, showing overall a mild (subpercent) dependence on the location of
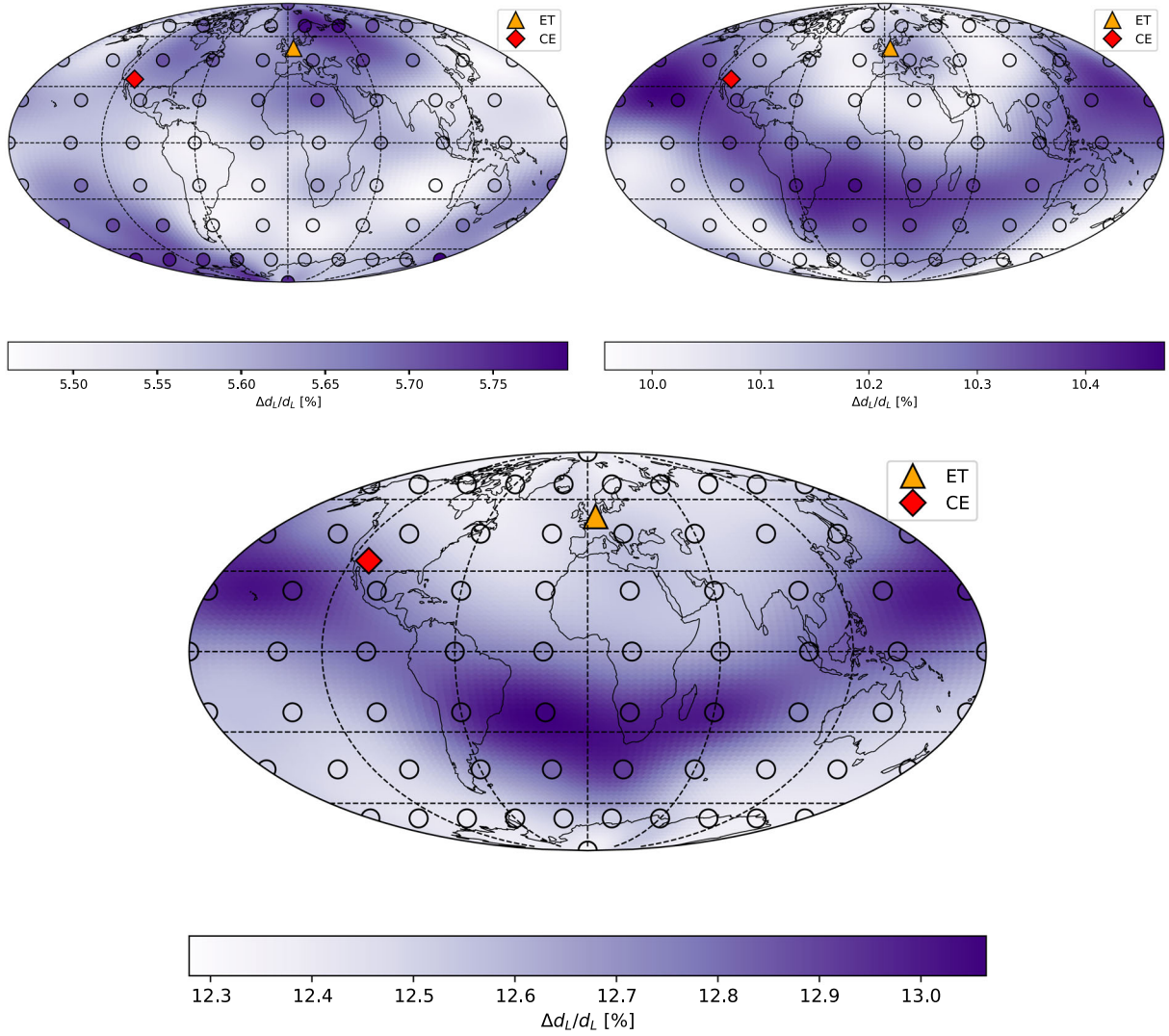
FIG. 13.   Luminosity distance uncertainty of a network of three detectors (ET + CE + ET) averaged over source location, depending on the location of the second ET-like detector. Empty circles denote the 90 trial locations of the third detector, while the first ET and the CE detector are denoted, respectively, by a yellow triangle and red diamond. The three figures refer to a redshift $z = 0.1$, 0.5, 1, respectively, moving clockwise from top left.

the third detector. When dealing with three detectors, the relative measurement error on Δd_L depend very mildly on the source sky location, as shown by Fig. 20.

D. Impact of ι distribution and type of network on d_L uncertainty

Beside the obvious importance of the number and quality of detectors in the network, another important feature in the forecast of luminosity distance uncertainty is the *source distribution of inclination angles*, for which we adopted the three distribution functions in Fig. 10.

Note that it is not *a priori* clear what distribution will be seen by a 3G detector. While 2G ones are likely to see a distribution of small values for $\min(\iota, \pi - \iota)$, which give larger SNRs, since 3G detector will have a much larger

reach, they should in principle see a distribution closer to the isotropic one, as observed in [76,77]. However, the selection of *bright* standard sirens may bias the observation towards GW signals accompanied by short GRB, which are expected to be somehow beamed [23], hence more likely to be observed for small ι or $\pi - \iota$. On the other hand, short GRBs do not have good sky localization, which can be achieved at high degree of accuracy with optical counterparts like kilonovae, that are broadly expected to be isotropically emitting [78], and hence can support the expectation of a $\sin \iota$, isotropic distribution of sources.

We then summarize the result for the average d_L uncertainty for six different network of detectors: {ET, CE, CE + CE, ET + CE, ET + ET, ET + ET + CE} given the three different ι source distributions. The ι prior at recovery is chosen to be equal to the injected cutoff
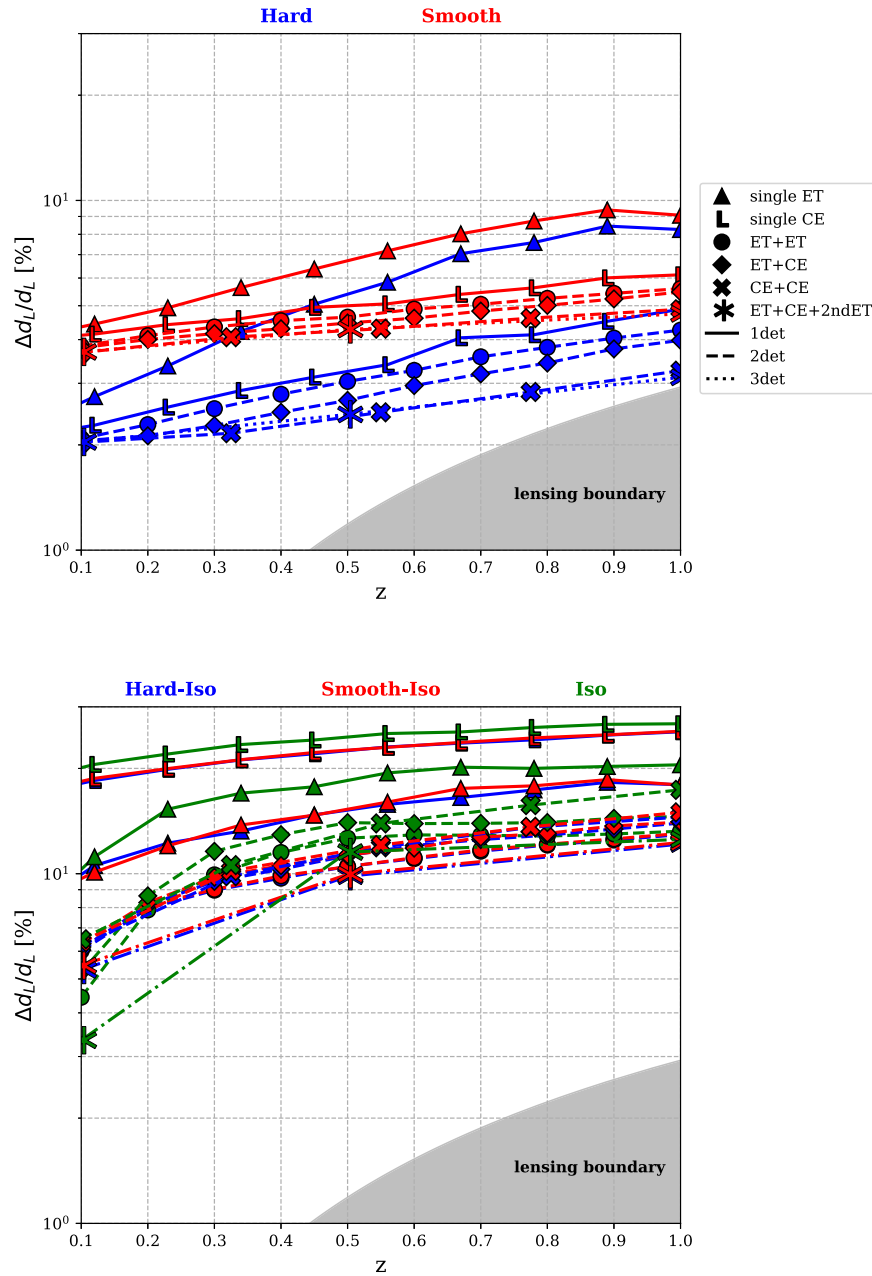
FIG. 14.   Average distance measure error for various network of ET- and CE-like detectors as a function of redshift. The top graph shows the case of anisotropic distribution of inclination angles with prior at recovery. The bottom one shows the case of isotropic prior at recovery for all cases of ι injection distribution. See Fig. 10 for ι injection distributions (*hard, smooth, iso*).

distribution in the top plot of Fig. 14 and equal to an isotropic distribution in the bottom plot of the same figure.

From Fig. 14, we can draw interesting conclusions about the impact of the underlying inclination angle distributions and on the network features:

(1) In the case GW sources are characterized by "polar" inclination angles, i.e., small values of either ι or $\pi - \iota$, folding in such information at recovery leads to a significant improvement (up to a factor ~ 5) in d_L uncertainty determination. This is shown by the

comparison of the two plots in Fig. 14, where on the top plot, results are shown for injections distributed at small angles only (see "hard" and "smooth cutoff" in Fig. 10, using a recovery prior equal to injection distribution), and the bottom plot has been obtained using an isotropic prior at recovery, i.e., $\propto \sin \iota$. In particular, in the top plot, there is virtually no difference between the cases of hard and smooth cutoff, and also little difference between injections isotropic on the sphere or concentrated near the poles.

(2) As expected, adding a 3G detector to an existing network is beneficial to the d_L recovery precision but less obvious is the effect of adding a CE-like detector instead of an ET-like one. A CE-CE network can ensure roughly the same precision as $ET + ET + CE$, and it is slightly better in terms of d_L precision than a $ET + CE$ system, showing that the better design sensitivity we adopted for the CE compared to the ET, see left plot in Fig. 2, has a non-negligible effect when it comes to forming a network which has already good sky coverage, like, e.g., a network of two L-shaped detectors.

For the dispersion of $\Delta d_L/d_L$ values, see Fig. 19 in the three detector case of Fig. 14.

Overall, uncertainty in d_L smoothly increases with redshift, with the results in broad agreement with the cumulative distributions shown in [53], see also [79] for binary black holes, even if a more detailed comparison is not possible as here, differently from there, we present results broken at a specific redshift. For the reader interested in comparing with present observations, we report in Appendix D the same result of Fig. 14 superimposed to scatter plots of luminosity distance uncertainties obtained with 2G detectors Advanced LIGO and Virgo in their first three observation runs [1–3] and with the *standard candle* catalog [80].

Note that for a wide and sensitive enough detector network $(ET + ET + CE)$ or $CE + CE$, it is possible at a moderately high redshift (~ 0.7) to almost reach the limit on d_L uncertainty imposed by the *lensing* intervening between source and observer, whose approximate value can be found in [81]. Also in [82], it is argued that with two or three 3G detectors working at design sensitivity, it may be worth including delensing in the analysis of the signals, anticipating to 3G detectors what was foreseen for space interferometers [83]. Note while some present estimate indicate that having an EM counterpart of a GW detection may be challenging for source at redshift larger than ~ 0.7 [37], there exist large uncertainties for the expected reach of next decades target-of-opportunity searches.

IV. CONCLUSIONS

With the goal of contributing to the use of gravitational wave signals from coalescing binaries as standard sirens to reconstruct the cosmic expansion history of the Universe, we analyzed the projected uncertainty measures of luminosity distances of third generation detectors. Observatories like the triangular Einstein Telescope, with arms at $60°$, and the L-shaped Cosmic Explorer, with arms at $90°$, are currently planned to start taking data just over a decade from now, but some of their features, like the exact location and topology, have not been finalized yet.

Luminosity distance precision measurement affects directly the measure of cosmological parameters, but luminosity distance correlates with a relatively large number of angular variables defining the relative location and orientation of source and detector. Such correlations can degrade the expected precision measurements, e.g., the one relying on a Fisher matrix approximation, thus requiring a numerical Bayesian framework for a consistent analysis. For the sake of definiteness, we focused on bright standard sirens of binary neutron stars, for which a host galaxy can be identified and sky localization obtained with negligible error, thus reducing the extrinsic angular variables to correlate with distance, to inclination, polarization, and phase shift. We neglect arrival time and extrinsic parameters like masses, which can be constrained with high accuracy from the GW phasing, and spins that are expected to be small for neutron star binaries giving rise to bright standard sirens.

We have neglected completely the effect of possible tidal deformation of neutron stars, which demand an accurate modeling of the waveform close to the merger, that is way beyond the scope of our work.

Our main results can be summarised as follows:

(1) While the presence of bimodality in the luminosity distance (d_L) versus inclination (ι) angle distribution is a well-known feature of detections by single L-shaped interferometers, we have quantitatively linked such impossibility to separate individual polarization contributions to a single scalar parameter, the ϵ_D first introduced in [60] (simply ϵ in this work). This parameter relates to the information of how much the subdominant polarization is present in the combined detector output. In particular, we have shown that detectors like the ones forming a triangular interferometer, which cover all sky localizations without blind directions, have $\epsilon < 1$ for virtually all of the sky, and they can present bimodality in $d_L - \iota$ recovery only for specific directions with $\epsilon \sim 1$.

(2) Another well-known feature of d_L vs ι uncertainty is the reduced error uncertainty for $\iota \to \pi/2$ for triangular interferometers. We found that this is a generic feature ascribable to an improved precision in the determination of the *polarization* angle, whose better constrained values are correlated with d_L measures.

(3) We have shown quantitative measures of d_L uncertainties for a variety of networks made of up to three third generation detectors. Besides qualitative results presented in plots, we showed that given a network of at least two misaligned detectors, which then have virtually no blind spots in the sky, the best way to increase the precision measurement is to add a more sensitive detector, rather than adding an equally performing one, even if with more arms. Moreover, we have shown that with three detectors, one can almost reach the measurement error level set by lensing, which start to be at the percent level from $z \gtrsim 0.6$.

(4) We have quantified how the inclination angle distribution affect the d_L uncertainty measures, with the result that knowing the underlying ι distribution can improve up to a factor 5 the luminosity distance uncertainty.

Obvious generalizations of the present work include to explore the nonsymmetric mass and spinning case. However, apart for the case of precessing binaries, which however are not expected for bright standard sirens [84], these features are expected to induce quantitative, rather than qualitative, changes of the results obtained here. One feature that could change the picture substantially is instead given by matter/tidal effects of a neutron star, which are relevant and close to the merger phase. Such effects are not only relevant for understanding the state of matter at high density inside the neutron stars but have a nontrivial impact on cosmological parameter estimation, as they introduce into the phasing of the gravitational waveform a term that depends explicitly on redshift [34]. This would give a handle to estimate redshift with gravitational information alone, which however require accurate development of accurate and exhaustive matter waveforms; see, e.g., [85] for a database.

APPENDIX A: POLARIZATION ANGLE

The radiation frame relative to the ith detector is defined, taking the $\hat{z}_{\rm rad}$ axis along the line pointing from the source to the observer ($\hat{N}$) and the $\hat{x}_{\rm rad}$ axis in the $\hat{z}_i - \hat{z}_{\rm rad}$ plane, being $\hat{z}_i$ the unit vector normal to the plane of the detector; see Fig. 3 for detector and radiation geometry.

The polarization angle ψ_i is then conventionally defined as the angle from $\hat{x}_{\rm rad}$ to the line of *ascending nodes*, which is determined by the unit vector parallel to $\hat{N} \times \hat{L}$, being $\hat{L}$ the unit vector parallel to the source angular momentum.

One then has

$$\hat{x}_{i,\rm rad} \equiv \frac{\hat{z}_i - (\hat{z}_i \cdot \hat{N})\hat{N}}{|\hat{z}_i - (\hat{z}_i \cdot \hat{N})\hat{N}|},$$

$$\hat{y}_{i,\rm rad} \equiv \hat{N} \times \hat{x}_{i,\rm rad}, \tag{A1}$$

and

$$\cos\psi = \hat{x}_{i,\rm rad} \cdot \frac{\hat{N} \times \hat{L}}{|\hat{N} \times \hat{L}|},$$

$$\sin\psi = \hat{y}_{i,\rm rad} \cdot \frac{\hat{N} \times \hat{L}}{|\hat{N} \times \hat{L}|}, \tag{A2}$$

from which it follows,

$$\tan\psi_i = \frac{(\hat{N} \times \hat{z}_i) \cdot (\hat{N} \times \hat{L})}{z_i \cdot (\hat{N} \times \hat{L})}$$

$$= \frac{\hat{L} \cdot [\hat{z}_i - (\hat{z}_i \cdot \hat{N})\hat{N}]}{\hat{z}_i \cdot (\hat{N} \times \hat{L})}. \tag{A3}$$

In the specific case when $\hat{L} \| \hat{N}$, the polarization angle ψ_i is not defined, as it is degenerate with a rotation in the plane of the orbit. The polarization angle is also undefined if $\hat{z} \| \hat{N}$, in which case one cannot define the radiation triad.

Note that the angles ι, ψ_i, with $\cos\iota \equiv \hat{L} \cdot \hat{N}$, determine the polar angles of $\hat{L}$, whose explicit components in the reference frame where $\hat{N} \| \hat{z}$ and $\hat{z}_i$ is in the $\hat{x} - \hat{z}$ plane, are

$$\hat{L} = (\sin\iota \sin\psi_i, -\sin\iota \cos\psi_i, \cos\iota), \qquad \hat{N} \| \hat{z}. \tag{A4}$$

We denote by α, β the polar angles defining $\hat{N}$, (α is the right ascension and the declination angle δ is related to β via $\delta = \pi/2 - \beta$) in the frame in which the reference vector $\hat{z}_i = (0,0,1)$,

$$\hat{N} = (\sin\beta \cos\alpha, \sin\beta \sin\alpha, \cos\beta), \qquad \hat{z}_i \| \hat{z}. \tag{A5}$$

The transformation taking from the source frame to the radiation frame is $R_z(\psi - \pi/2)R_y(\iota)R_z(\phi)$, and the one taking $\hat{N}$ from the form (A5) to the canonical form (0,0,1) is $[R_z(\alpha)R_y(\beta)]^{-1}$.

For a detector at latitude λ and longitude u, with $\hat{N}$ given by Eq. (A5), one has

$$\hat{z}_i = (\cos\lambda \cos u, \cos\lambda \sin u, \sin\lambda),$$

$$\hat{x}_i = (\cos\lambda \cos u - \cos\alpha \cos\beta \sin\lambda \sin\beta - \cos\lambda \cos(u-\alpha) \cos\alpha \sin^2\beta,$$

$$\cos\lambda \sin u - \sin\alpha \cos\beta \sin\lambda \sin\beta - \cos\lambda \cos(u-\alpha) \sin\alpha \sin^2\beta, \sin\lambda \sin^2\beta - \cos\lambda \cos(u-\alpha) \cos\beta \sin\beta)/\mathcal{N},$$

$$\mathcal{N}^2 \equiv 1 - [\cos\beta \sin\lambda + \cos\lambda \cos(u-\alpha) \sin\beta]^2, \tag{A6}$$
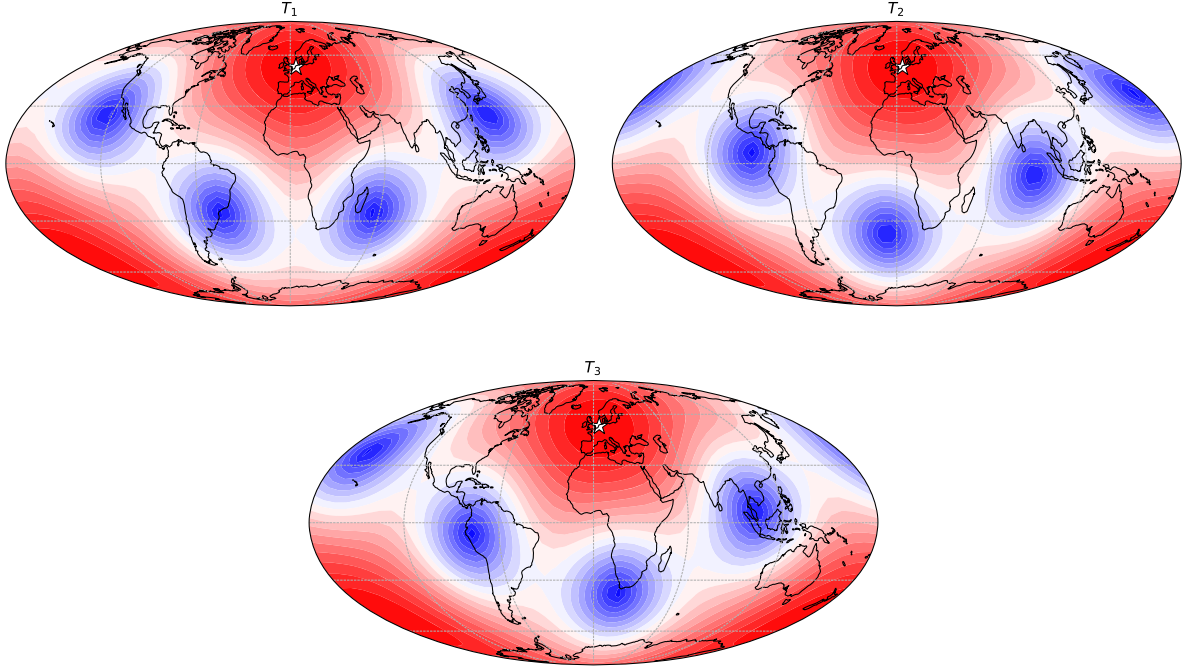
FIG. 15.   Quadratic sum of pattern function $(f_+^2 + f_\times^2)^{1/2}$ for each of the three component of a triangular interferometer with arms at 60°. The blind spots of each individual interferometer lie in the plane of the detector.

and one can then find that $\psi_i = \psi_0 + \delta\psi_i$ where $\delta\psi_i$ is determined as

$$\mathcal{N}\cos\delta\psi_i = \sin\lambda\sin\beta - \cos\lambda\cos(u-\alpha)\cos\beta,$$
$$\mathcal{N}\sin\delta\psi_i = -\cos\lambda\sin(u-\alpha), \tag{A7}$$

which shows that $\delta\psi_i$ depends only on the location of the source and not on the reference polarization angle ψ_0, as stated in Sec. II.

We conclude this appendix by reporting the explicit expression of the angle $\bar\psi$ defined in Eq. (19),

$$\cos 4\bar\psi = \frac{\Xi_{++} - \Xi_{\times\times}}{\Xi_0},$$

$$\sin 4\bar\psi = \frac{2\Xi_{+\times}}{\Xi_0},$$

$$\Xi_0^2 \equiv \Xi_{++}^2 + \Xi_{\times\times}^2 + 4\Xi_{+\times}^2 - 2\Xi_{++}\Xi_{\times\times}, \tag{A8}$$

and finally, the relationship between $\Xi_{dt_i AB}$ and its diagonal version (29),

$$\bar\Xi_{d_i t AB} = M_{AC}^{-1} \Xi_{d_i t CD} M_{DB}, \tag{A9}$$

with

$$M_{AB} = \begin{pmatrix} \frac{F_+\sin(2\psi_t)-F_\times\cos(2\psi_t)}{F_+\cos(2\psi_t)+F_\times\sin(2\psi_t)} & \frac{F_+\cos(2\psi)+F_\times\sin(2\psi)}{F_\times\cos(2\psi)-F_+\sin(2\psi)} \\ 1 & 1 \end{pmatrix}. \tag{A10}$$

APPENDIX B: DEGENERACY BETWEEN d_L AND ι

According to the explanation given in Sec. II, see point 3 below Eq. (21), the presence of bimodality is unavoidable (for ι sufficiently distant from the value $\pi/2$) for $\epsilon \sim 1$. Note that the blind zones of the individual interferometers making the ET are very close together; see Fig. 15, so that for those specific source position the response of ET is not too dissimilar from the response of L-shaped detector.

Taking, e.g., the case of 2G detectors, the two LIGOs are almost perfectly aligned, making $\epsilon \sim 1$ for most of the sky; the addition of Virgo and KAGRA will not change drastically the situation as they have larger spectral noise sensitivity, see Fig. 16 for the σ and ϵ maps and Fig. 17 for 2G detector design spectral noise sensitivities.

APPENDIX C: RELATION TO DOMINANT POLARIZATION FRAME

In this work, we relied on the parametrization leading to expression (21) that we borrowed from [60]. In [87], a similar parametrization has been introduced, identifying the *dominant polarization frame*, i.e., the *radiation* frame for which the detector network is maximally sensitive to the $+$ polarization, by using the general property that different radiation frames are related by a shift in the polarization angle, i.e., a rotation around the propagation direction. The detector signal is then parametrized in [87] as

HL

HLV

HLVK
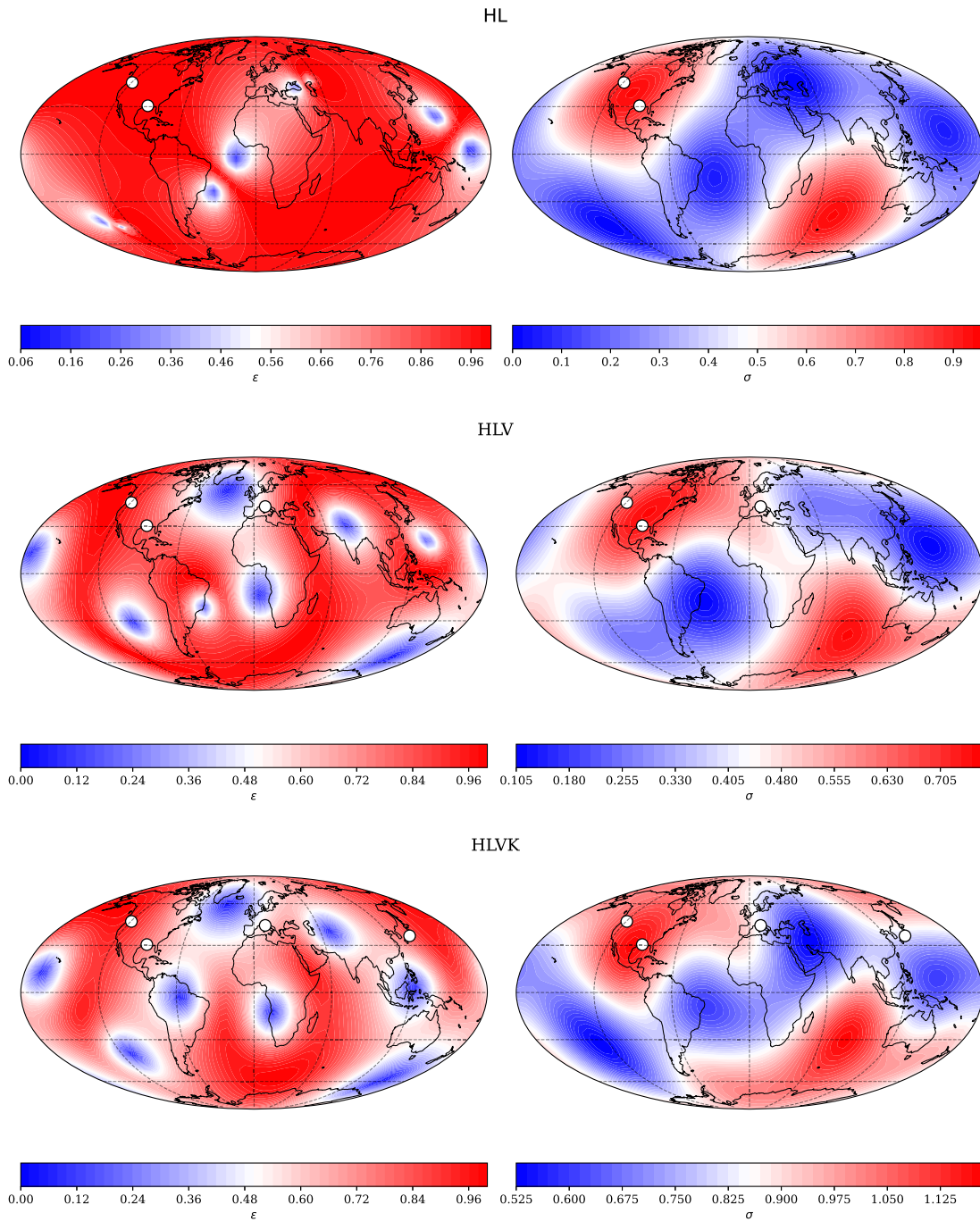
FIG. 16. Values of σ and ϵ for various networks of 2G detectors, spectral noise curves used are displayed in Fig. 17.
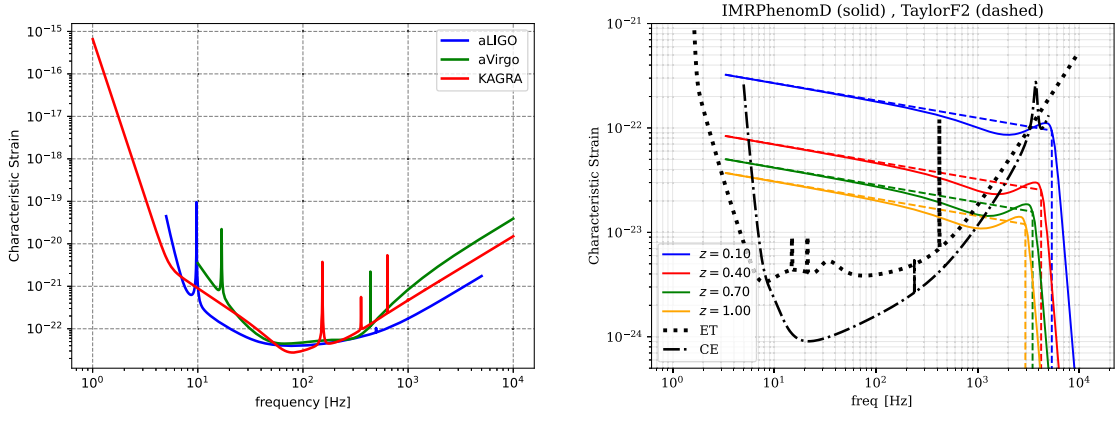
FIG. 17.   Left: Characteristic strain $\sqrt{fS_n}$ used to generate maps in Fig. 16, from [86]. Right: Examples of TaylorF2 (dashed) and IMRPhenomD (solid) waveforms for total mass $3M_\odot$ and equal binary component masses.

$$h_{\text{det}} = g_k(h_+ + \epsilon_k h_\times), \qquad (C1)$$

leading to the following mapping of these coefficients into our σ, ϵ:

$$g_k = \sigma\sqrt{1 + \epsilon},$$
$$\epsilon_k = \sqrt{\frac{1 - \epsilon}{1 + \epsilon}}. \qquad (C2)$$

APPENDIX D: 3G LUMINOSITY DISTANCE UNCERTAINTY COMPARISON WITH 2G DETECTORS AND STANDARD CANDLES

As a comparison with luminosity distance uncertainties obtained with 2G GW detectors and standard candles, we report in Fig. 18 luminosity distance uncertainties from our 3G projections superimposed with the catalogues in [1–3] and [80].

Finally, we report here the sky distribution of the injections used for the three detector analysis of Sec. III C 2 (ET + CE + ET), which highlight the location selection effect of the SNR threshold at large distances.
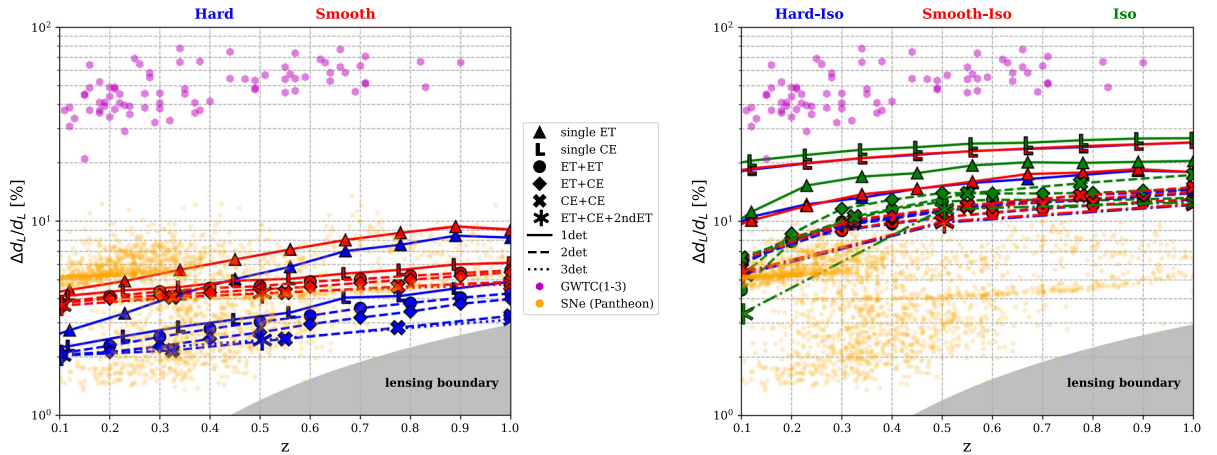
FIG. 18.   Same as in Fig. 14, with uncertainties in luminosity distance of 2G detections from [1–3] and standard sirens from [80] added.
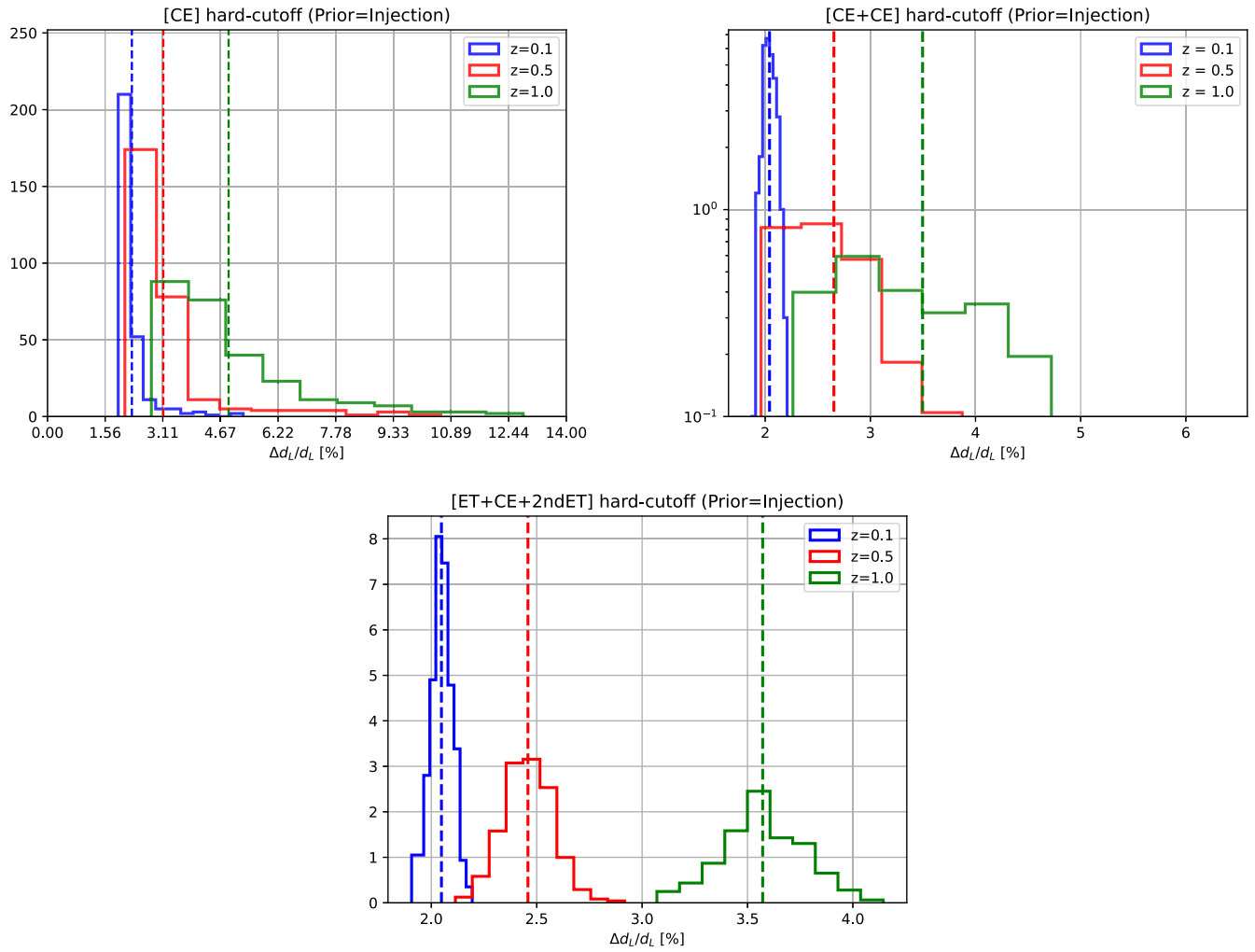
FIG. 19. Histograms representing the dispersions of $\Delta d_L/d_L$ measurements for sample 1,2, and 3 detector case of Fig. 14. *Hard cutoff* refers to the ι distributions of the injections as per Fig. 10.
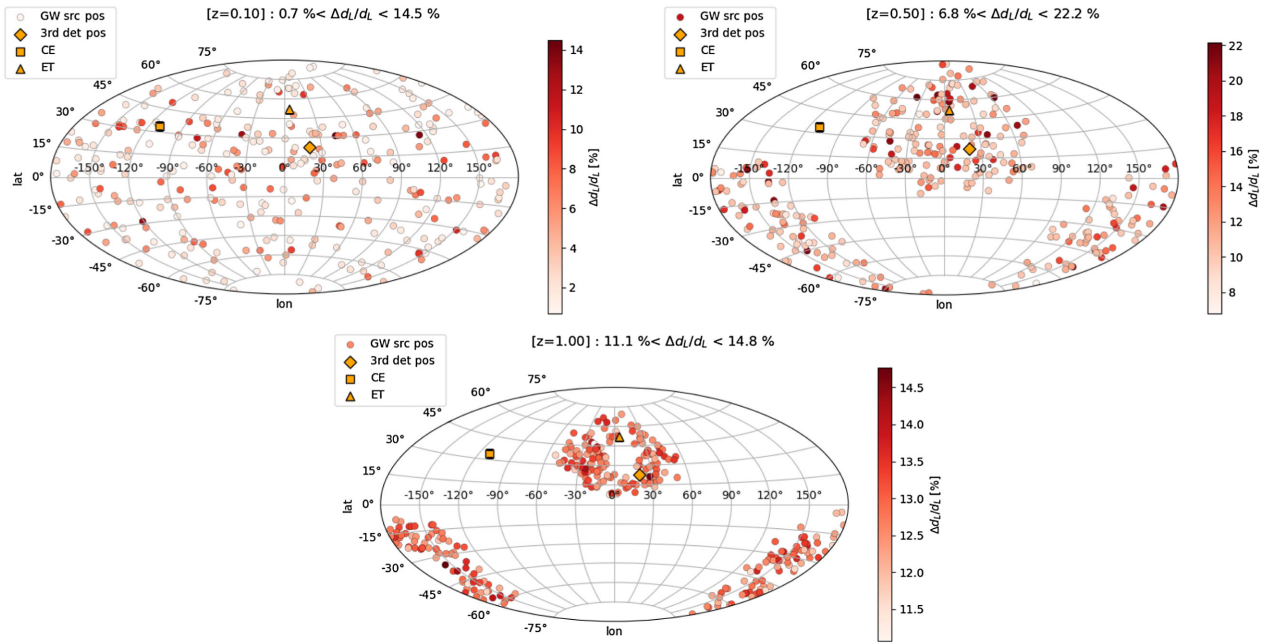
FIG. 20. Sky distribution of above threshold events for the three detector network (ET + CE + ET) of Sec. III C 2, showing how threshold cut selects source sky regions.

[1] B. P. Abbott *et al.* (LIGO Scientific and Virgo Collaborations), Phys. Rev. X **9**, 031040 (2019).

[2] R. Abbott *et al.* (LIGO Scientific and Virgo Collaborations), Phys. Rev. X **11**, 021053 (2021).

[3] R. Abbott *et al.* (LIGO Scientific, VIRGO, and KAGRA Collaborations), arXiv:2111.03606 [Phys. Rev. X (to be published)].

[4] R. Abbott *et al.* (LIGO Scientific and Virgo Collaborations), Phys. Rev. D **103**, 122002 (2021).

[5] R. Abbott *et al.* (LIGO Scientific, VIRGO, and KAGRA Collaborations), arXiv:2112.06861 [Phys. Rev. D (to be published)]

[6] B. P. Abbott *et al.* (LIGO Scientific, Virgo, 1M2H, Dark Energy Camera GW-E, DES, DLT40, Las Cumbres Observatory, VINROUGE, and MASTER Collaborations), Nature (London) **551**, 85 (2017).

[7] B. P. Abbott *et al.* (LIGO Scientific, Virgo, and VIRGO Collaborations), Astrophys. J. **909**, 218 (2021).

[8] R. Abbott *et al.* (LIGO Scientific, VIRGO, and KAGRA Collaborations), Astrophys. J. **949**, 76 (2023).

[9] J. Aasi *et al.* (LIGO Scientific Collaboration), Classical Quantum Gravity **32**, 074001 (2015).

[10] F. Acernese *et al.* (VIRGO Collaboration), Classical Quantum Gravity **32**, 024001 (2015).

[11] B. P. Abbott *et al.* (KAGRA, LIGO Scientific, and VIRGO Collaborations), Living Rev. Relativity **21**, 3 (2018).

[12] T. Akutsu *et al.* (KAGRA Collaboration), Prog. Theor. Exp. Phys. **2021**, 05A101 (2021).

[13] B. F. Schutz, Nature (London) **323**, 310 (1986).

[14] D. E. Holz and S. A. Hughes, Astrophys. J. **629**, 15 (2005).

[15] B. McKernan, K. E. S. Ford, W. Lyra, and H. B. Perets, Mon. Not. R. Astron. Soc. **425**, 460 (2012).

[16] I. Bartos, B. Kocsis, Z. Haiman, and S. Márka, Astrophys. J. **835**, 165 (2017).

[17] M. J. Graham, K. E. S. Ford, B. McKernan, N. P. Ross, D. Stern, K. Burdge, M. Coughlin, S. G. Djorgovski, A. J. Drake, D. Duev *et al.*, Phys. Rev. Lett. **124**, 251102 (2020).

[18] B. McKernan, K. E. S. Ford, I. Bartos, M. J. Graham, W. Lyra, S. Marka, Z. Marka, N. P. Ross, D. Stern, and Y. Yang, Astrophys. J. Lett. **884**, L50 (2019).

[19] S. S. Kimura, K. Murase, and I. Bartos, Astrophys. J. **916**, 111 (2021).

[20] A. Palmese, M. Fishbach, C. J. Burke, J. T. Annis, and X. Liu, Astrophys. J. Lett. **914**, L34 (2021).

[21] W. E. East, L. Lehner, S. L. Liebling, and C. Palenzuela, Astrophys. J. Lett. **912**, L18 (2021).

[22] E. E. Flanagan and T. Hinderer, Phys. Rev. D **77**, 021502 (2008).

[23] B. D. Metzger and E. Berger, Astrophys. J. **746,** 48 (2012).

[24] G. Dálya, G. Galgóczi, L. Dobos, Z. Frei, I. S. Heng, R. Macas, C. Messenger, P. Raffai, and R. S. de Souza, Mon. Not. R. Astron. Soc. **479,** 2374 (2018).

[25] B. P. Abbott *et al.* (LIGO Scientific and Virgo Collaborations), Phys. Rev. Lett. **119,** 161101 (2017).

[26] W. Del Pozzo, Phys. Rev. D **86,** 043011 (2012).

[27] M. Soares-Santos *et al.* (DES, LIGO Scientific, and Virgo Collaborations), Astrophys. J. Lett. **876,** L7 (2019).

[28] R. Gray *et al.*, Phys. Rev. D **101,** 122001 (2020).

[29] S. Mukherjee, B. D. Wandelt, S. M. Nissanke, and A. Silvestri, Phys. Rev. D **103,** 043520 (2021).

[30] C. C. Diaz and S. Mukherjee, Mon. Not. R. Astron. Soc. **511,** 2782 (2022).

[31] L.-G. Zhu, Y.-M. Hu, H.-T. Wang, J.-d. Zhang, X.-D. Li, M. Hendry, and J. Mei, Phys. Rev. Res. **4,** 013247 (2022).

[32] H. Leandro, V. Marra, and R. Sturani, Phys. Rev. D **105,** 023523 (2022).

[33] J. M. Ezquiaga and D. E. Holz, Astrophys. J. Lett. **909,** L23 (2021).

[34] C. Messenger and J. Read, Phys. Rev. Lett. **108,** 091101 (2012).

[35] H.-Y. Chen, M. Fishbach, and D. E. Holz, Nature (London) **562,** 545 (2018).

[36] T. Regimbau, M. Evans, N. Christensen, E. Katsavounidis, B. Sathyaprakash, and S. Vitale, Phys. Rev. Lett. **118,** 151105 (2017).

[37] E. Belgacem, Y. Dirian, S. Foffa, E. J. Howell, M. Maggiore, and T. Regimbau, J. Cosmol. Astropart. Phys. 08 (2019) 015.

[38] J. M. S. de Souza, R. Sturani, and J. Alcaniz, J. Cosmol. Astropart. Phys. 03 (2022) 025.

[39] S. Vitale and C. Whittle, Phys. Rev. D **98,** 024029 (2018).

[40] P. Madau and M. Dickinson, Annu. Rev. Astron. Astrophys. **52,** 415 (2014).

[41] M. Punturo *et al.*, Classical Quantum Gravity **27,** 194002 (2010).

[42] M. Evans *et al.*, arXiv:2109.09882.

[43] M. Maggiore, *Gravitational Waves: Volume 1: Theory and Experiments*, Gravitational Waves (Oxford University Press, Oxford, 2008), ISBN 9780198570745, https://books.google .com.br/books?id=AqVpQgAACAAJ.

[44] H.-Y. Chen, D. E. Holz, J. Miller, M. Evans, S. Vitale, and J. Creighton, Classical Quantum Gravity **38,** 055010 (2021).

[45] V. Srivastava, D. Davis, K. Kuns, P. Landry, S. Ballmer, M. Evans, E. D. Hall, J. Read, and B. S. Sathyaprakash, Astrophys. J. **931,** 22 (2022).

[46] M. Evans, J. Jarms, and S. Vitale, Technical Report No. LIGO Document P1600143, 2016, https://dcc.ligo .org/LIGO-P1600143/public.

[47] N. D. Lillo, A. Singha, A. Utina, and S. Hild, Technical Report, ET docs, 2019, https://apps.et-gw.eu/tds/ql/? c=14313.

[48] T. A. Apostolatos, C. Cutler, G. J. Sussman, and K. S. Thorne, Phys. Rev. D **49,** 6274 (1994).

[49] L. Vainshtein and V. Zubakov, *Extraction of Signals from Noise: By L.A. Wainstein and V.D. Zubakov* (Dover, New York, 1970), https://books.google.com.br/books? id=PTPSzAEACAAJ.

[50] L. S. Finn and D. F. Chernoff, Phys. Rev. D **47,** 2198 (1993).

[51] B. J. Owen, Phys. Rev. D **53,** 6749 (1996).

[52] M. Burgay *et al.*, Nature (London) **426,** 531 (2003).

[53] F. Iacovelli, M. Mancarella, S. Foffa, and M. Maggiore, Astrophys. J. **941,** 208 (2022).

[54] E. E. Flanagan and S. A. Hughes, Phys. Rev. D **57,** 4566 (1998).

[55] B. Goncharov, A. H. Nitz, and J. Harms, Phys. Rev. D **105,** 122007 (2022).

[56] E. D. Hall and M. Evans, Classical Quantum Gravity **36,** 225002 (2019).

[57] L. Sun *et al.*, Classical Quantum Gravity **37,** 225008 (2020).

[58] B. Abbott *et al.* (LIGO Scientific Collaboration), Nucl. Instrum. Methods Phys. Res., Sect. A **517,** 154 (2004).

[59] V. Varma, P. Ajith, S. Husa, J. C. Bustillo, M. Hannam, and M. Pürrer, Phys. Rev. D **90,** 124004 (2014).

[60] C. Cutler and E. E. Flanagan, Phys. Rev. D **49,** 2658 (1994).

[61] S. A. Usman, J. C. Mills, and S. Fairhurst, Astrophys. J. **877,** 82 (2019).

[62] S. Hild *et al.*, Classical Quantum Gravity **28,** 094013 (2011).

[63] J. Veitch and W. Del Pozzo, Technical Report No. LIGO Document T1300326, 2013.

[64] J. Veitch *et al.*, Phys. Rev. D **91,** 042003 (2015).

[65] C. L. Rodriguez, B. Farr, V. Raymond, W. M. Farr, T. B. Littenberg, D. Fazi, and V. Kalogera, Astrophys. J. **784,** 119 (2014).

[66] G. Ashton *et al.*, Astrophys. J. Suppl. Ser. **241,** 27 (2019).

[67] P. Mukherjee, D. Parkinson, and A. R. Liddle, Astrophys. J. Lett. **638,** L51 (2006).

[68] J. Skilling, Bayesian Anal. **1,** 833 (2006).

[69] B. S. Sathyaprakash and B. F. Schutz, Living Rev. Relativity **12,** 2 (2009).

[70] S. Husa, S. Khan, M. Hannam, M. Pürrer, F. Ohme, X. Jiménez Forteza, and A. Bohé, Phys. Rev. D **93,** 044006 (2016).

[71] S. Khan, S. Husa, M. Hannam, F. Ohme, M. Pürrer, X. Jiménez Forteza, and A. Bohé, Phys. Rev. D **93,** 044007 (2016).

[72] E. Chassande-Mottin, K. Leyde, S. Mastrogiovanni, and D. A. Steer, Phys. Rev. D **100,** 083514 (2019).

[73] S. Vitale and H.-Y. Chen, Phys. Rev. Lett. **121,** 021303 (2018).

[74] H.-Y. Chen, S. Vitale, and R. Narayan, Phys. Rev. X **9,** 031028 (2019).

[75] V. Alfradique, M. Quartin, L. Amendola, T. Castro, and A. Toubiana, Mon. Not. R. Astron. Soc. **517,** 5449 (2022).

[76] B. F. Schutz, Classical Quantum Gravity **28,** 125023 (2011).

[77] S. Vitale, Phys. Rev. D **94,** 121501 (2016).

[78] P. S. Cowperthwaite *et al.*, Astrophys. J. Lett. **848,** L17 (2017).

[79] S. Vitale and M. Evans, Phys. Rev. D **95,** 064052 (2017).

[80] D. M. Scolnic *et al.* (Pan-STARRS1 Collaboration), Astrophys. J. **859,** 101 (2018).

[81] W. Zhao, C. Van Den Broeck, D. Baskaran, and T. Li, Phys. Rev. D **83,** 023005 (2011).

[82] X. Shan, C. Wei, and B. Hu, Mon. Not. R. Astron. Soc. **508,** 1253 (2021).

[83] N. Tamanini, C. Caprini, E. Barausse, A. Sesana, A. Klein, and A. Petiteau, J. Cosmol. Astropart. Phys. 04 (2016) 002.

[84] S. Vitale, R. Lynch, J. Veitch, V. Raymond, and R. Sturani, Phys. Rev. Lett. **112**, 251101 (2014).

[85] A. Gonzalez *et al.*, Classical Quantum Gravity **40**, 085011 (2023).

[86] M. Evans, R. Sturani, S. Vitale, and E. Hall, Technical Report No. LIGO DCC T1500293-v13, 2020, https://dcc .ligo.org/LIGO-T1500293/public.

[87] S. Klimenko, S. Mohanty, M. Rakhmanov, and G. Mitselmakher, Phys. Rev. D **72**, 122002 (2005).